

# Circularization of Tidally Disrupted Stars around Spinning Supermassive Black Holes

Kimitake Hayasaki<sup>1,2,3\*</sup>, Nicholas Stone<sup>3,4</sup> and Abraham Loeb<sup>3</sup>

<sup>1</sup>*Department of Astronomy and Space Science, Chungbuk National University, Cheongju 361-763, Korea*

<sup>2</sup>*Korea Astronomy and Space Science Institute, Daedeokdaero 776, Yuseong, Daejeon 305-348, Korea*

<sup>3</sup>*Harvard-Smithsonian Center for Astrophysics, 60 Garden Street, Cambridge, MA 02138, USA*

<sup>4</sup>*Department of Astronomy, Columbia University, 550 W. 120th Street, New York, NY 10027, USA*

## ABSTRACT

We study the circularization of tidally disrupted stars on bound orbits around spinning supermassive black holes by performing three-dimensional smoothed particle hydrodynamic simulations with Post-Newtonian corrections. Our simulations reveal that debris circularization depends sensitively on the efficiency of radiative cooling. There are two stages in debris circularization if radiative cooling is inefficient: first, the stellar debris streams self-intersect due to relativistic apsidal precession; shocks at the intersection points thermalize orbital energy and the debris forms a geometrically thick, ring-like structure around the black hole. The ring rapidly spreads via viscous diffusion, leading to the formation of a geometrically thick accretion disc. In contrast, if radiative cooling is efficient, the stellar debris circularizes due to self-intersection shocks and forms a geometrically thin ring-like structure. In this case, the dissipated energy can be emitted during debris circularization as a precursor to the subsequent tidal disruption flare. The circularization timescale is remarkably long in the radiatively efficient cooling case, and is also sensitive to black hole spin. Specifically, Lense-Thirring torques cause dynamically important nodal precession, which significantly delays debris circularization. On the other hand, nodal precession is too slow to produce observable signatures in the radiatively inefficient case. Since the stellar debris is optically thick and its photon diffusion time is likely longer than the timescale of shock heating, our inefficient cooling scenario is more generally applicable in eccentric tidal disruption events (TDEs). However, in parabolic TDEs for  $M_{\text{BH}} \gtrsim 2 \times 10^6 M_{\odot}$ , the spin-sensitive behavior associated with efficient cooling may be realized.

**Key words:** accretion, accretion discs – black hole physics – galactic: nuclei – hydrodynamics

## 1 INTRODUCTION

Most galaxies are thought to harbor supermassive black holes (SMBHs) with masses from  $10^5$  to  $10^9 M_{\odot}$  at their centers (Kormendy & Richstone 1995; Kormendy & Ho 2013). This is inferred from observing proper motions of stars bound to the SMBHs (Schödel et al. 2002), measuring stellar velocity dispersions around SMBHs (Magorrian et al. 1998) or detecting radiation emitted from gas accreting onto the SMBHs (Miyoshi et al. 1995). In the last of these signatures, continuous accretion from a gas reservoir in active galactic nuclei (AGNs) produces intense radiation and powerful outflows and jets. On the other hand, gas accretion proceeds quiescently, at a significantly lower rate, in the centers of inactive galaxies. The gas poor environment

surrounding these SMBHs is not accompanied by significant emission (Genzel et al. 2003).

Tidal disruption events (TDEs) provide a distinctive opportunity to probe dormant SMBHs at the centres of such inactive galaxies. Most TDEs take place when a star at large separation ( $\sim 1$  pc) is perturbed onto a parabolic orbit approaching close enough to the SMBH to be ripped apart by the tidal forces, at the radius  $r_t \simeq (M_{\text{BH}}/m_*)^{1/3} r_* = 24 (M_{\text{BH}}/10^6 M_{\odot})^{-2/3} (m_*/M_{\odot})^{-1/3} (r_*/R_{\odot}) r_s$ . Here we denote SMBH mass with  $M_{\text{BH}}$ , stellar mass with  $m_*$  and radius with  $r_*$ , and the Schwarzschild radius with  $r_s = 2GM_{\text{BH}}/c^2$ , where  $G$  and  $c$  are Newton’s constant and the speed of light, respectively. The subsequent accretion of stellar debris falling back to the SMBH produces a characteristic flare with a luminosity large enough to exceed the Eddington luminosity for a time scale of weeks to month (Rees 1988; Evans & Kochanek 1989). Recent observations of Swift

\* E-mail: kimi@cgnu.ac.kr

J164449.3+573451 showed that relativistic jets are associated with some fraction of TDEs (Bloom et al. 2011; Burrows et al. 2011; Zauderer et al. 2011; Levan et al. 2011). Candidates for TDEs have also been observed at X-ray, ultraviolet, and optical wavebands (Komossa & Bade 1999; Gezari et al. 2012; Arcavi et al. 2014; Holoien et al. 2014; Vinkó et al. 2015), with inferred event rates of  $10^{-5}$  per year per galaxy (Donley et al. 2002; van Velzen & Farrar 2014), although the observed light curves and spectra (Gezari et al. 2012) do not always match the simplest theoretical expectations (Loeb & Ulmer 1997; Lodato & Rossi 2011; Strubbe & Quataert 2011).

Black hole spin is one of two fundamental quantities characterizing astrophysical black holes, which inevitably acquire spin angular momentum as a result of standard mass accretion or chaotic accretion (King & Pringle 2006). Measuring black hole spins has proven much more difficult than black hole mass estimation, because the dynamical effects of spin occur much closer to the event horizon. Since an accretion disk can get closer to the black hole when the black hole is spinning (Bardeen et al. 1972), a detailed spectral analysis of disk X-ray emission can determine the black hole spin (Tanaka et al. 1995). Such indirect spin measurements have been so far made for about 30 SMBHs (Miller 2007), and recently indicated that the SMBH at the centre of the nearby galaxy NGC 1365 has at least 84% of the maximum theoretically allowed value (Risaliti et al. 2013).

SMBH spins are difficult to measure, but are of significant astrophysical importance. Spin amplitude and direction significantly affect the efficiency for converting rest mass energy into radiation. While the mass-to-energy conversion efficiency reaches  $\approx 42\%$  for an extreme Kerr black hole in a prograde rotation, it is only  $\approx 4\%$  for the retrograde case (Kato et al. 2008), suggesting a wide range of bolometric disk luminosities depending on the relative inclination of disk and SMBH spin. A SMBH-disk system can also work as an engine to convert the black hole’s rotational energy into outflows and jets (Blandford & Znajek 1977; Koide et al. 2002). The outflow efficiency depends on spin magnitude and direction via a large-scale magnetic flux threading the black hole and the disk (Tchekhovskoy et al. 2012).

It is still theoretically uncertain whether such jets will align with the black hole spin axis, with the angular momentum vector of the accretion disk, or with some other aspect of the magnetic field geometry (Stone & Loeb 2012a). A misaligned accretion disk will undergo differential precession due to Lense-Thirring frame dragging. While a geometrically thin disk warps by the Bardeen-Petterson effect (Bardeen & Petterson 1975), a geometrically thick disk can precess as a rigid-body rotator, as has been seen in general relativistic magneto-hydrodynamic (GRMHD) simulations (Fragile et al. 2007). Very recent GRMHD simulations have also shown that a highly magnetized geometrically thick disk can warp due to electromagnetic torques (McKinney et al. 2013).

The present spin of a SMBH records the history of gas accretion and mergers with other black holes, and statistical samples of SMBH spins encode valuable information on the growth history of SMBHs in the universe (Volonteri et al. 2005; Berti & Volonteri 2008). The SMBHs in most AGN are thought to have accreted sufficient gas in their active phase to be rotating near the extreme Kerr limit (Doeleman et al. 2012), although events of randomly oriented gas

clump accretion might be able to produce black holes that rotate much more slowly. In contrast to generally aligned prograde accretion in AGN, spinning SMBHs undergoing TDEs can rotate either retrograde or prograde with respect to inflowing gas, with a full range of possible inclinations for the transient accretion disk. TDEs therefore act as natural laboratories for testing theories about accretion and jet launching physics over a full range of prograde and retrograde inclination angles.

Our simulations have focused primarily on tidal disruption of stars with eccentric, rather than parabolic (Evans & Kochanek 1989; Ayal et al. 2000; Ramirez & Rosswog 2009; Guillochon et al. 2014), centre of mass trajectories. Although the standard two-body scattering mechanism for generating TDEs (Magorrian & Tremaine 1999; Merritt & Wang 2004) predicts effectively parabolic trajectories ( $1 - e_* \lesssim 10^{-6}$ ), other mechanisms can feed stars to SMBHs at lower eccentricities. Among these non-standard sources of TDEs, the most promising are binary SMBHs, a recoil accompanying a SMBH merger, and the tidal separation of binary stars. Recent numerical simulations have shown that observable properties of these “eccentric” TDEs significantly deviate from those of standard TDEs; in particular, the rate of mass return is substantially increased by being cut off at a finite time, rather than continuing indefinitely as a power law decay (Hayasaki et al. 2013). Because of their naturally limited dynamic range, simulations of eccentric tidal disruption were the first to capture relativistic circularization of debris around SMBHs, which is extremely computationally challenging for the canonical parabolic case. These simulations found that circularization is driven by general relativistic pericentre shift, which causes shocks to form at stream self-intersections. The orbital energy dissipated at these self-intersections subsequently circularizes the debris into a more compact accretion disk (Hayasaki et al. 2013). This is in contrast to past Newtonian simulations of circularization for parabolic orbits around intermediate mass black holes ( $\sim 10^3 M_\odot$ ), where purely hydrodynamic effects circularize tidally stretched debris (Ramirez & Rosswog 2009); although these are expected to be ineffective for SMBH-like mass ratios (Guillochon et al. 2014).

The primary motivation for this work is to investigate the effect of SMBH spin on debris circularization. We test the hypothesis that nodal precession due to the Lense-Thirring effect can delay the onset of stream self-intersections and strongly retard formation of a luminous accretion disk (Cannizzo et al. 1990; Kochanek 1994). If proven true, TDE circularization delays could be used as probes of SMBH spin. Such delays could also decrease the average luminosity of many TDEs; if spin-induced circularization delay is common but not universal, it would produce a bimodality in TDE optical emission that could explain a discrepancy between theoretically predicted and observationally inferred TDE rates (Stone & Metzger 2014).

In this paper, we study the circularization of a tidally disrupted star on an eccentric orbit around a spinning SMBH. In section 2, we describe our numerical approach, focusing on the Post-Newtonian corrections we make use of. In section 3, we examine the results of our numerical simulations in two limiting regimes: one is the radiatively efficient cooling case, in which the photon diffusion time is much shorter than the energy dissipation timescale. In the

opposite scenario, where the radiative cooling is inefficient, the debris circularization proceeds in a qualitatively different way. In section 4, we examine the effect of black hole spin on debris circularization, and the nodal precession of the newly formed accretion disk by the Lense-Thirring effect. Finally, section 5 is devoted to summary and discussion of our scenario.

## 2 METHODS

We start by describing our numerical methods, with a special focus on how to treat relativistic effects in the numerical code, and summarize the setup of our physical and numerical models. First, we describe our procedures for numerically modeling the tidal disruption of stars on bound orbits. The simulations presented below were performed with a three-dimensional (3D) Smoothed Particle Hydrodynamics (SPH) code, which is a particle method that divides the fluid into a set of particles, and is flexible in setting various initial configurations. The code is based on a version originally developed by Benz (1990); Benz et al. (1990); and Bate et al. (1995).

The SPH equations are composed of a mass conservation equation, a momentum equation with the SPH standard artificial viscosity, and an energy equation. Their details will be described later, in section 2.1. These equations, with the standard cubic-spline kernel, are integrated using a second-order Runge-Kutta-Fehlberg integrator with individual time steps for each particle and a variable smoothing length (Bate et al. 1995), resulting in enormous computational savings when a large range of dynamical timescales are involved.

The variable smoothing length scheme we used gives appropriate spatial resolution in our code, but we ignore the term proportional to the gradient of the smoothing length. This term is introduced for calculating the gradient of fluid properties when the smoothing length is varied in space and time, and is important for ensuring energy conservation if the gradient of any physical quantities varies over a shorter scale than the smoothing length (see Bate 1995 for a review). In our simulations, the specific energy is well conserved for all the models. This shows that the term plays no crucial role in our simulations.

We have performed 3D SPH simulations self-consistently modeling a star from before its entry into the tidal sphere up to late times, when the stellar debris has circularized into a disk. We model general relativistic effects, including leading order SMBH spin corrections, by incorporating Post-Newtonian (PN) forces up to 2PN into the SPH code. We have run ten pairs of simulations of tidal disruption events with different parameters. The common parameters through all of simulations are following:  $m_* = 1M_\odot$ ,  $r_* = 1R_\odot$ ,  $M_{\text{BH}} = 10^6 M_\odot$ ,  $\gamma = 5/3$ , and a unit of run time  $P_* = 2\pi\Omega_*^{-1} = 2\pi\sqrt{r_*^3/Gm_*} \simeq 2.8$  hr. The total number of SPH particles used in each simulation is 100K, where  $K=1000$ . We also adopt the standard value of the artificial viscosity parameters:  $\alpha_{\text{SPH}} = 1$  and  $\beta_{\text{SPH}} = 2$  through all the simulations.

Table 1 summarizes each model. Models 1-4 show the eccentric TDEs around non-spinning SMBHs with  $(e, \beta) = (0.9, 1)$ ,  $(0.8, 1)$ ,  $(0.7, 1)$ , and  $(0.7, 2)$ . Models 5 and 6 have the same simulation parameters as Model 4, except that

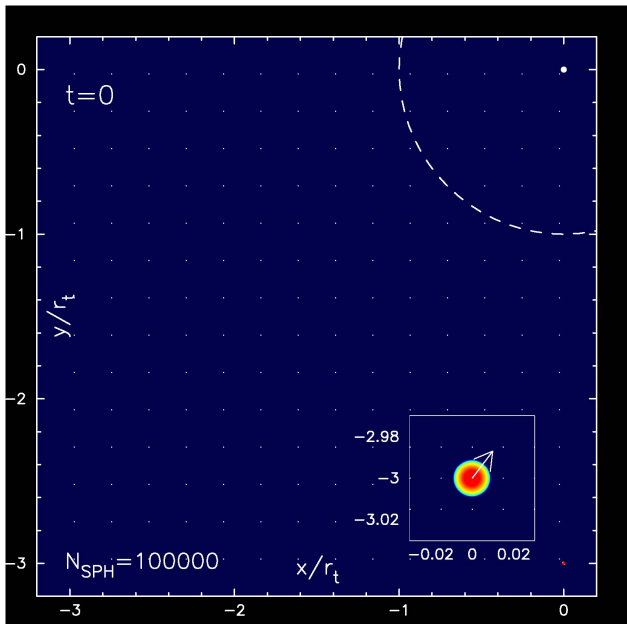


**Figure 1.** Initial configuration of our simulations. The dashed white circle and its central small white dot show the tidal disruption radius  $r_t$  and the black hole at the origin, respectively. The run time  $t$  in units of  $P_*$  and the number of SPH particles  $N_{\text{SPH}}$  are annotated at the top-left corner and the bottom-right corner, respectively. Both the  $x$ -axis and the  $y$ -axis are normalized by  $r_t$ . The star is initially located at  $(0.3 r_t, 0)$  for Models 1-3, and is zoomed into the small square inside the main panel. There, the white small arrow indicates the velocity vector of the star.

the black hole is spinning with spin parameters  $\chi = 0.9$  for Model 5 and  $\chi = -0.9$  for Model 6. Both models have an inclination angle  $i = 0^\circ$  between the spin angular momentum and the axis perpendicular to the orbital plane of the stellar debris. Models 7 and 8 have the same parameters as Model 6 but for  $i = 90^\circ$  for Model 7 and  $i = 45^\circ$  for Model 8, respectively. Model 9 has the same parameters as Model 8 but for  $\chi = 0.9$ . Model 10 has the same simulation parameters as Model 1 but for  $(e, \beta) = (0.8, 5)$ , and has been performed to compare with Model 2a of Hayasaki et al. (2013) (see section 3.2). Each of these ten sets of simulation parameters has been run twice, with two different equations of state (adiabatic and polytropic, discussed in more detail in section 3).

### 2.1 Treatment of relativistic effects in SPH

The formalism of Post-Newtonian (PN) hydrodynamics was constructed by Blanchet et al. (1990) for the approximate treatment of relativistic effects in a non-covariant framework. Their formalism is applicable to a moderately relativistic self-gravitating fluid (with gravitational radiation reaction, if desired), so long as the PN parameter  $GM_{\text{BH}}/Rc^2$  (for a typical spatial scale  $R$ ) never exceeds  $\approx 10\%$ . It is not, however, simple to implement this formalism into existing Newtonian SPH codes.

For a typical TDE with an orbital speed  $v$ , the PN parameter is estimated to be  $\mathcal{O}(v^2/c^2) = 10^{-2}$  at the tidal disruption radius. The magnitude of the self-gravitating potential and thermal energy of the star can be similarly

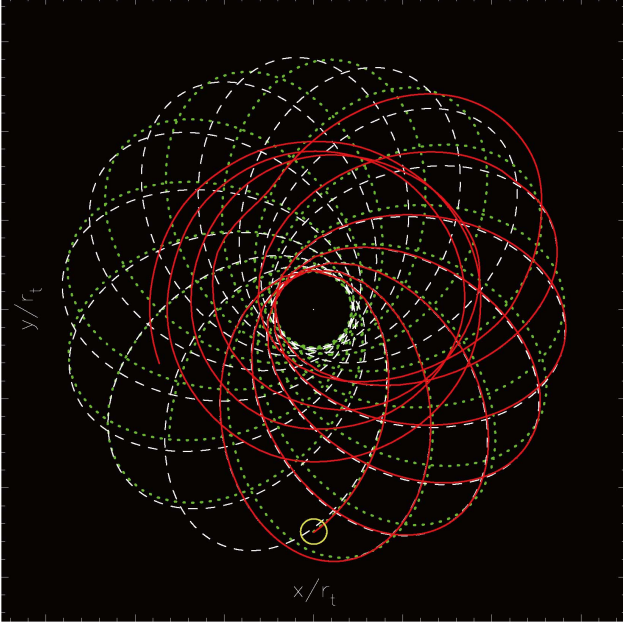


**Figure 2.** Orbits of two test particles and one SPH particle (from our full disruption simulation with the adiabatic equation of state) around a spinning SMBH. The parameters of Model 5 are adopted for the three particles. Each axis is normalized by the tidal disruption radius. The initial positions of the particles are located at the center of the small yellow circle. The central white point shows the black hole with  $(\chi, i) = (0.9, 0^\circ)$ . The solid red and dashed white lines show the motion of a SPH particle and a test particle in the gravitational potential with Post-Newtonian corrections (up to 2PN). The dotted line denotes an orbit of a test particle moving in the Kerr metric.

parameterized to be  $\mathcal{O}((v^2/c^2)(m_*/M_{\text{BH}})^{2/3}) = 10^{-6}$  and  $\mathcal{O}(c_s^2/c^2) = 10^{-5}$  where  $c_s$  is the sound speed (for a stellar temperature  $\sim 10^7$  K), respectively. These order of magnitude estimates show that even the lowest PN order terms for stellar self-gravitation and thermal energy can be self-consistently neglected, even if up to 2PN precision in the black hole's gravity is desired. Because we only need to modify the SMBH potential, and can continue to treat hydrodynamics and gas self-gravity in a Newtonian fashion, it becomes much simpler to implement the PN formalism into our SPH code.

In order to treat approximately relativistic effects such as pericentre shift and spin-induced precession, we have incorporated acceleration terms corrected by the Post-Newtonian approximations into the momentum equation of SPH particles. The detailed formulae can be seen in Appendix A.

## 2.2 Initial conditions

We have performed two-stage simulations: a star is first modeled as a polytropic gas sphere in hydrostatic equilibrium. The tidal disruption process is then simulated by setting the star in motion through the gravitational field of a black hole. In our simulations, the black hole is represented by a sink particle with the appropriate gravitational mass  $M_{\text{BH}}$ . All gas particles that fall within a specified accretion radius are accreted by the sink particle. We set the accre-

tion radius of the black hole as the radius of the marginally stable orbit for the non-spinning black hole (Bardeen et al. 1972):  $r_{\text{ms}} \simeq 0.12 r_t$ , in all the models.

The initial position and velocity of the star is given by that of a test particle orbiting around the black hole. In the test-particle limit, the specific energy and angular momentum with PN corrections are given from equations (A7) and (A9) by

$$\epsilon_{\text{tp}} = \frac{E_i(\mathbf{r}_{\text{BH}} = 0, \mathbf{v}_{\text{BH}} = 0)}{m_i}, \quad (1)$$

$$\mathbf{j}_{\text{tp}} = \frac{\mathbf{J}_i(\mathbf{r}_{\text{BH}} = 0, \mathbf{v}_{\text{BH}} = 0)}{m_i}, \quad (2)$$

where the index  $i$  refers to a given SPH particle, and  $\mathbf{r}_{\text{BH}}$  and  $\mathbf{v}_{\text{BH}}$  are the position and velocity vector of the black hole particle, respectively. This energy and angular momentum should approximately equal their respective Newtonian analogues at a distance far away from the black hole. Given an initial position and desired pericenter distance, we numerically solve for an initial velocity vector using the PN constants of motion. The initial velocity and position vector in our simulation models are summarized in Table 2. The number of initial SPH particles  $N_{\text{SPH}}$  are 100K for all the models. Figure 1 shows an initial configuration of our simulations for Models 1-3.

Figure 2 shows orbits of two test particles and one SPH particle (from our full disruption simulation with the adiabatic equation of state) around a spinning SMBH. The solid red and dashed white lines show the motion of a SPH particle and a test particle in the gravitational potential with Post-Newtonian corrections (up to 2PN). The dotted line denotes an orbit of a test particle moving in the Kerr metric. The orbit of the test particle in the 2PN potential deviates slightly from that of the Kerr metric. It is initially identical with the orbit of the SPH particle for the first five orbits, but the two diverge afterwards because of hydrodynamic forces on the SPH particle.

## 2.3 Errors of energy and angular momentum conservation

In order to check convergence of energy and angular momentum conservation with PN corrections, we numerically solve the two-body problem with PN corrections in a test particle limit by using a fourth-order Runge-Kutta method. While the energy and angular momentum are well conserved in the case of a circular binary, they oscillate with time in an eccentric binary case (but remain conserved in a time-averaged sense). The oscillation amplitude grows with increasing orbital eccentricity of the test particle and increasing ratio of the tidal disruption radius to pericentre distance of the test particle.

In Table 2, we compare the error levels of energy and angular momentum conservation between the test-particle simulations and the SPH simulations. Each error level is measured by

$$\delta\epsilon = \frac{\bar{\epsilon} - \epsilon_*}{\epsilon_*}, \quad \delta j = \frac{\bar{j} - j_*}{j_*}, \quad (3)$$

where  $\bar{\epsilon}$  and  $\bar{j}$  are the time-averaged and number-averaged PN values of specific energy and angular momentum during the first ten orbits, while  $\epsilon_*$  and  $j_*$  are the Newtonian



**Table 1.** Tabulated simulation parameters. The first column shows each simulated model number. The second to seventh columns are the penetration factor  $\beta = r_p/r_t$ , the initial orbital eccentricity  $e_*$ , the initial semi-major axis  $a_*$ , the radial distance between the black hole and the initial position of the star, the specific orbital binding energy of the star  $\epsilon_* = -(1/2)\beta(1 - e_*)\epsilon_t$  where  $\epsilon_t = GM_{\text{BH}}/r_t \simeq 1.9 \times 10^{19} \text{ [erg/g]}$ , and the black hole spin parameter  $\chi$  (with values between 0 and 1), respectively. The eighth column indicates the angle between the black hole spin axis and the axis perpendicular to the orbital plane of the stellar debris. The ninth and tenth columns are the periods of the most tightly and loosely bound orbits, respectively (see equations (15) and (16)). The eleventh column shows each termination time normalized by  $P_* = 2\pi\sqrt{r_t^3/GM_{\text{BH}}} \simeq 2.8 \text{ hr}$ . The last two columns describe the number of SPH particles at the end of simulations for radiatively efficient ( $N_{\text{eff}}$ ) and inefficient cooling ( $N_{\text{ineff}}$ ) cases.

Model	$\beta$	$e_*$	$a_* [r_t]$	$r_0 [r_t]$	$\epsilon_* [\epsilon_t]$	$\chi$	$i$	$t_{\text{mtb}} [P_*]$	$t_{\text{mlb}} [P_*]$	$t_{\text{end}} [P_*]$	$N_{\text{eff}}$	$N_{\text{ineff}}$
1	1	0.9	10	3	-0.05	0	0°	11	44	100	99142	96854 ( $t_{\text{end}} = 80$ )
2	1	0.8	5	3	-0.1	0	0°	4	13	100	99540	91140
3	1	0.7	10/3	3	-0.15	0	0°	2.2	6.7	100	99980	85675
4	2	0.7	5/3	2.5	-0.3	0	0°	0.76	2.3	40	99830	74520
5	2	0.7	5/3	2.5	-0.3	0.9	0°	0.76	2.3	40	99824	81610
6	2	0.7	5/3	2.5	-0.3	-0.9	0°	0.76	2.3	40	99687	71148
7	2	0.7	5/3	2.5	-0.3	-0.9	90°	0.76	2.3	40	99805	72233
8	2	0.7	5/3	2.5	-0.3	-0.9	45°	0.76	2.3	40	99869	69329
9	2	0.7	5/3	2.5	-0.3	0.9	45°	0.76	2.3	40	99907	82574
10	5	0.8	1	1.8	-0.5	0	0	0.35	1.03	10	99632	—

**Table 2.** Initial conditions and errors for our simulations. The first column shows each simulated model. The second and third columns denote the initial position and velocity vector for each model. The normalization of the velocity is given by  $v_t = \sqrt{GM_{\text{BH}}/r_t}$ . The fourth and fifth column show the energy conservation error and angular momentum conservation error of a test particle, respectively. The last two columns describe the energy conservation error and angular momentum conservation error of a SPH particle, respectively.

Model	$\mathbf{r}_0 [r_t]$	$\mathbf{v}_0 [v_t]$	$\delta\epsilon_{\text{tp}} [\%]$	$\delta j_{\text{tp}} [\%]$	$\delta\epsilon_{\text{SPH}} [\%]$	$\delta j_{\text{SPH}} [\%]$
1	(0.0, -3.0, 0.0)	(0.447, 0.589, 0.0)	1.0	0.08	0.054	0.041
2	(0.0, -3.0, 0.0)	(0.436, 0.512, 0.0)	1.0	0.07	0.041	0.026
3	(0.0, -3.0, 0.0)	(0.506, 0.474, 0.0)	0.27	0.02	0.16	0.05
4	(0.0, -2.5, 0.0)	(0.359, 0.25, 0.0)	4.0	0.45	0.25	0.02
5	(0.0, -2.5, 0.0)	(0.359, 0.251, 0.0)	3.5	0.35	0.12	0.31
6	(0.0, -2.5, 0.0)	(0.359, 0.248, 0.0)	4.8	2.8	0.38	0.23
7	(0.0, -2.5, 0.0)	(0.359, 0.249, 0.0)	4.2	0.45	0.25	0.4
8	(0.0, -2.5, 0.0)	(0.359, 0.251, 0.0)	4.5	2.0	0.19	0.19
9	(0.0, -2.5, 0.0)	(0.359, 0.249, 0.0)	3.5	0.18	0.31	0.6
10	(0.556, -1.71, 0)	(0.377, 0.1225, 0)	10.6	1.74	5.1	22.6

specific energy and angular momentum of the initially approaching star, respectively. Except for Model 10, the energy and angular momentum is well conserved at an error level of 2%.

### 3 STELLAR DEBRIS CIRCULARIZATION

Recent numerical simulations have shown that the pericentre shift of the stellar debris plays an essential role in quickly forming an accretion disk around a non-spinning SMBH, because it leads to debris orbit self-intersections, which dissipate energy in shocks and cause rapid circularization (Hayasaki et al. 2013). This work also showed that the angular momentum of the stellar debris is conserved during circularization. This angular momentum conservation allow us to estimate the circularization radius of the stellar debris, which is given by

$$r_c = a_*(1 - e_*^2) = \frac{1 + e_*}{\beta} r_t, \quad (4)$$

where  $a_*$ ,  $e_*$ , and  $\beta$  are the semi-major axis and orbital eccentricity of the initially approaching star, and the ratio of tidal disruption radius  $r_t$  to pericenter distance  $r_p = a_*(1 - e_*)$ , respectively. The specific binding energy of the stellar debris measured at the circularization radius can then be written as

$$\epsilon_c = -\frac{1}{2} \frac{\beta}{1 + e_*} \epsilon_t, \quad (5)$$

where  $\epsilon_t = GM_{\text{BH}}/r_t$  is a characteristic specific energy of the tidal disruption radius. On the other hand, the specific orbital energy of the initially approaching star is:

$$\epsilon_* = -\frac{1}{2} \beta (1 - e_*) \epsilon_t. \quad (6)$$

Note that the 1PN, 1.5PN, and 2PN order terms are proportional to  $(GM/r_t)/c^2 \sim 2.1\%$ ,  $(GM/r_t)^{3/2}/c^3 \sim 0.31\%$ , and  $(GM/r_t)^2/c^4 \sim 0.045\%$ , respectively, at the tidal disruption radius. This shows that equations (4)-(6) are typically corrected at the  $\sim 2.5\%$  level by our PN approaches.

The difference between  $m_*\epsilon_*$  and  $m_*\epsilon_c$  gives the maxi-

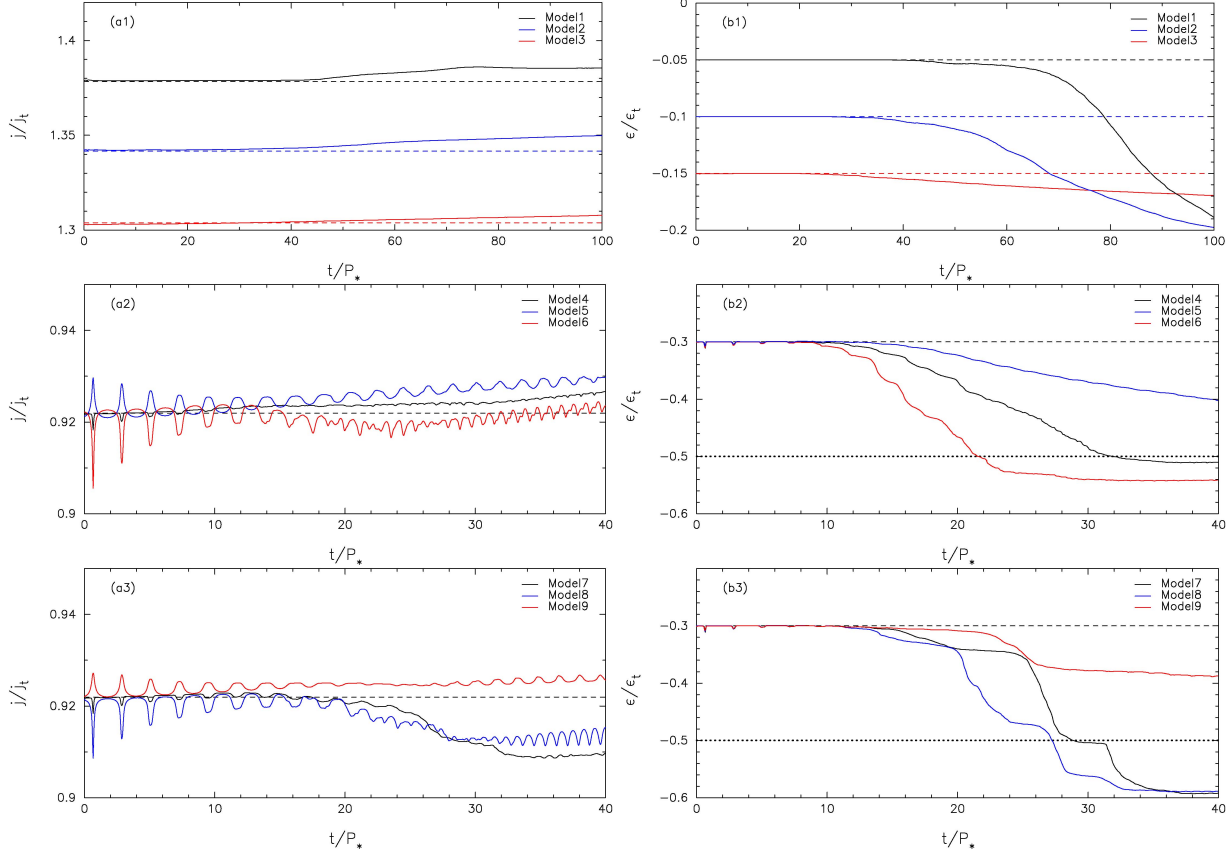


**Figure 3.** Evolution of the specific angular momentum and energy for Models 1-9 in the radiatively efficient cooling cases. These constants are averaged out per SPH particle. In panels (a1)-(a3), the black, blue, and red solid lines denote the specific angular momentum normalized by  $j_t = \sqrt{GM_{\text{BH}}r_t}$ . The corresponding dashed lines show the specific angular momentum of a test particle moving in a Newtonian potential,  $j_* = \sqrt{a_*(1-e_*^2)}$ . In panels (b1)-(b3), the black, blue, and red solid lines represent the specific binding energy normalized by  $\epsilon_t = GM_{\text{BH}}/r_t$ . The corresponding dashed lines show the Newtonian specific binding energy of a test particle,  $\epsilon_* = -(1/2)\beta(1-e_*)\epsilon_t$ . The dotted line shows the Newtonian specific binding energy measured at the tidal disruption radius. The run time  $t$  is in units of  $P_* = 2\pi\sqrt{r_t^3/GM} \simeq 2.8$  hr.

amount of binding energy potentially dissipated during debris circularization:

$$\delta\epsilon_{\text{max}} = m_*|\epsilon_* - \epsilon_c| = \frac{m_*}{2} \frac{\beta e_*^2}{(1+e_*)} \epsilon_t \simeq 1.9 \times 10^{52} [\text{erg}] \times \frac{\beta e^2}{(1+e)} \left(\frac{m_*}{M_\odot}\right)^{4/3} \left(\frac{r_*}{R_\odot}\right)^{-1} \left(\frac{M_{\text{bh}}}{10^6 M_\odot}\right)^{2/3} \quad (7)$$

It is crucial to consider where the dissipated energy goes during debris circularization. The photon diffusion timescale of the stellar debris is given by (Mihalas & Mihalas 1984)

$$t_{\text{diff}} = \frac{H}{c} \tau \simeq 6.1 \times 10^8 [\text{s}] \left(\frac{\kappa}{\kappa_{\text{es}}}\right) \left(\frac{\Sigma}{\Sigma_0}\right) \left(\frac{H}{\Delta r}\right) \left(\frac{r_*}{R_\odot}\right)^{-2} \times \left(\frac{m_*}{M_\odot}\right)^{5/3} \left(\frac{M_{\text{BH}}}{10^6 M_\odot}\right)^{-2/3} \left(\frac{r}{r_t}\right)^{-1}, \quad (8)$$

where  $H$ ,  $\kappa$ ,  $\Sigma$ , and  $\tau$  are the scale height, opacity, surface density, and optical depth of the stellar debris, respectively. The optical depth is approximately estimated to be

$$\tau = \kappa \rho H \sim \kappa \Sigma \simeq 2.6 \times 10^6 \left(\frac{\kappa}{\kappa_{\text{es}}}\right) \left(\frac{\Sigma}{\Sigma_0}\right) \left(\frac{r_*}{R_\odot}\right)^{-2} \left(\frac{m_*}{M_\odot}\right)^{5/3}$$

$$\times \left(\frac{M_{\text{BH}}}{10^6 M_\odot}\right)^{-2/3} \left(\frac{r}{r_t}\right)^{-1} \left(\frac{\Delta r}{r_t}\right)^{-1}, \quad (9)$$

where  $\kappa_{\text{es}} = 0.4 [\text{cm}^2 \text{g}^{-1}]$  is the opacity for electron scattering, and

$$\Sigma_0 \equiv \frac{m_*}{2\pi r \Delta r} \simeq 6.5 \times 10^6 [\text{g cm}^{-2}] \left(\frac{r_*}{R_\odot}\right)^{-2} \left(\frac{m_*}{M_\odot}\right)^{5/3} \times \left(\frac{M_{\text{BH}}}{10^6 M_\odot}\right)^{-2/3} \left(\frac{r}{r_t}\right)^{-1} \left(\frac{\Delta r}{r_t}\right)^{-1} \quad (10)$$

is the fiducial surface density, where  $r$  and  $\Delta r$  are the radial size and width of the debris ring, respectively. We note that the stellar debris is clearly optically thick. If the photon diffusion timescale is longer than the energy dissipation timescale (i.e. the debris circularization timescale), then radiative cooling is inefficient and dynamically unimportant. Otherwise, the radiative cooling can be efficient; the dynamical effect of this will be to reduce the thickness of the debris streams.

It is clear from equation (8) that in the eccentric TDEs we simulate,  $t_{\text{diff}}$  will always be very long compared to orbital timescales, and cooling will generally be radiatively

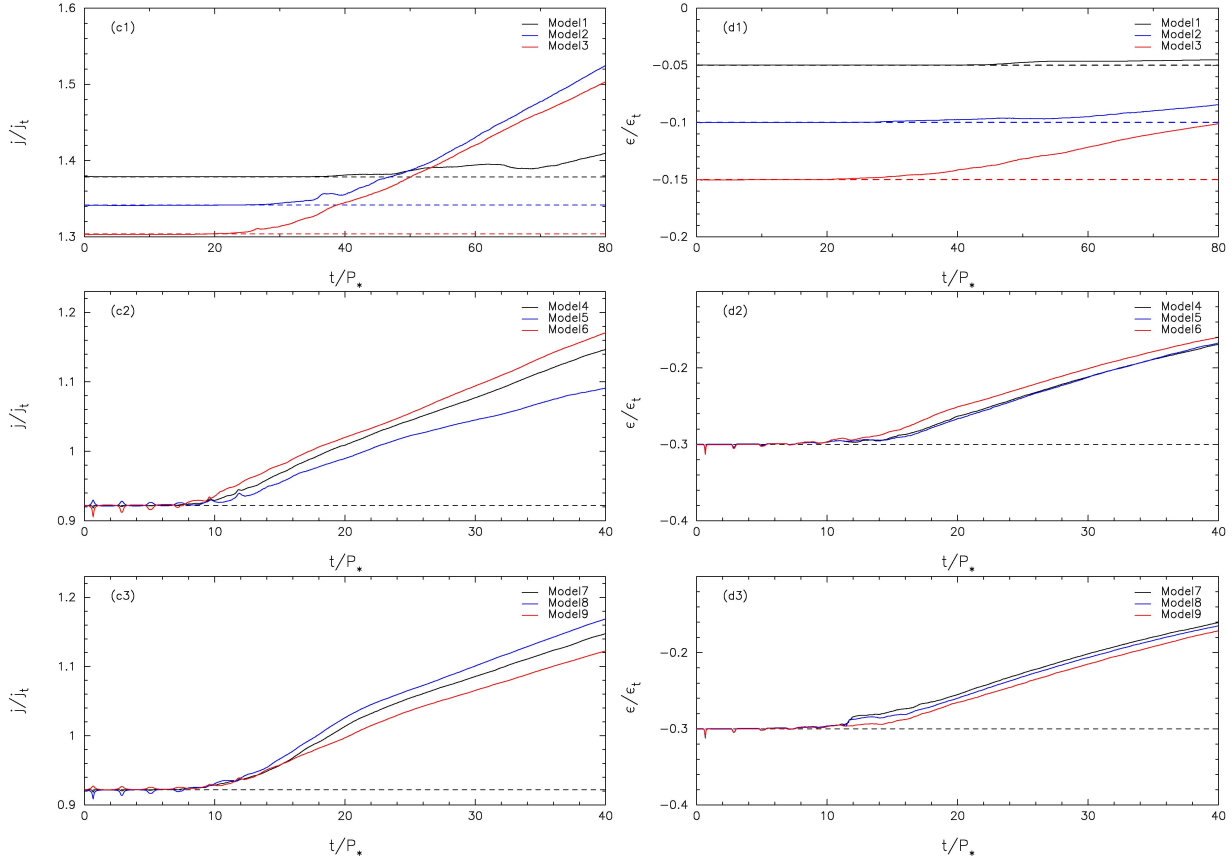


**Figure 4.** Evolution of the specific angular momentum and energy for Models 1-9 in the radiatively inefficient cooling cases. The figure formats are the same as Figure 3.

inefficient. However, this is not necessarily true for the parabolic ( $e_* \approx 1$ ) TDEs which dominate the event rate. If we approximate the frozen-in specific energy spread of  $e_* \approx 1$  tidal debris as (Stone et al. 2013)

$$\Delta\epsilon_t = \frac{GM_{\text{BH}} r_*}{r_t r_t}, \quad (11)$$

then we can calculate the fallback time with Kepler's third law for the most tightly bound debris to be

$$t_{\text{fb}} = \frac{1}{2\sqrt{2}} \left( \frac{M_{\text{BH}}}{m_*} \right)^{1/2} P_* = 3.5 \times 10^6 \text{ [s]} \left( \frac{M_{\text{BH}}}{10^6 M_\odot} \right)^{1/2} \times \left( \frac{m_*}{M_\odot} \right)^{-1} \left( \frac{r_*}{R_\odot} \right)^{3/2}. \quad (12)$$

We can estimate the regime where cooling is important by requiring  $t_{\text{diff}} < t_{\text{fb}}$ ; this is conservative because circularization likely takes several fallback times to complete. If we assume roughly cylindrical debris streams, with  $H = \Delta r$ , then factors of  $\Delta r$  cancel and we are left with a simple condition on the maximum extent of the debris stream,  $r$ , which we hereafter identify as debris apocenter  $r_a$ . Specifically,

$$\frac{r_a}{r_t} \gtrsim 1.7 \times 10^2 \left( \frac{\kappa}{\kappa_{\text{es}}} \right) \left( \frac{M_{\text{BH}}}{10^6 M_\odot} \right)^{-5/6} \left( \frac{r_*}{R_\odot} \right)^{-5/2} \left( \frac{m_*}{M_\odot} \right)^{7/3}. \quad (13)$$

This illustrates why eccentric TDEs should generally be in the radiatively inefficient limit, but if we substitute in the apocenter of the most tightly bound debris streams for

parabolic TDEs, we obtain the following condition for radiatively efficient cooling:

$$M_{\text{BH}} \gtrsim 1.6 \times 10^6 M_\odot \left( \frac{\kappa}{\kappa_{\text{es}}} \right)^{6/7} \left( \frac{r_*}{R_\odot} \right)^{-15/7} \left( \frac{m_*}{M_\odot} \right)^{16/7}. \quad (14)$$

Under our simplifying assumptions, radiative cooling will be, in general, likely to play some dynamical role for debris streams of parabolic TDEs. The radiative efficiency of these streams could be reduced if they cool to the point where bound-free absorption dominates electron scattering as a source of opacity (Kochanek 1994), but it could also be increased if magnetically driven turbulent advection of photons enhances cooling rates (Jiang et al. 2014).

Given the many uncertainties in this discussion, and the possible applicability of both regimes to parabolic TDEs, we present two extreme cases: one involves a set of radiatively efficient cooling simulations, where the entropy remains constant through the simulation, in the polytropic equation of state with  $\gamma = 5/3$ . The other involves the radiatively inefficient cooling simulations, where the entropy is locally increased with adiabatic equation of state but the total energy is conserved. The detailed parameters of ten (9+1) simulation models are shown in Table 1. Note that Model 10 is done for the purpose of comparison to the fiducial simulation model of Hayasaki et al. (2013), where the pseudo-Newtonian potential was adopted. Further details are described in section 3.2.

### 3.1 Radiatively efficient cooling cases

First, we describe the results of our radiatively efficient cooling simulations, which serve as one extreme of possible radiative cooling. Figure 3 shows the evolution of the specific angular momentum and specific energy in Models 1-9, which are averaged per SPH particle. Panels (b1)-(b3) show the evolution of the specific binding energy in Models 1-9. The thermal energy is estimated to be the order of  $10^{-5} \epsilon_t$  for all the models, and therefore it is negligibly small compared with the magnitude of the orbital binding energy. Panels (a1)-(a3) show the evolution of specific angular momentum per SPH particle. The small-amplitude oscillations seen there are due to the PN terms added in the SPH equation of motion. Equivalent errors are also seen in energy and angular momentum conservation for a test particle on an eccentric orbit moving under a gravitational potential with PN corrections. We compared these errors between the SPH simulations and the test particle integrations. The detailed results can be seen in columns 4-7 of Table 2 in Section 2.3. Note that the angular momentum of the SPH particles in all the models is conserved at a less than 2% error level through the simulations.

Figures 5-7 show a sequence of snapshots of the surface density of stellar debris, which is projected on the  $x$ - $y$  plane in a logarithmic scale, covering two orders of magnitude, for Models 1-3. Each figure progresses from panel (a) to panel (d) in chronological order. The central small point, dashed circle and white small arrows show the black hole, tidal disruption radius, and velocity field of the stellar debris, respectively. The run time is noted at the top-right corner in units of  $P_*$ , while the number of SPH particles is indicated at the bottom-right corner.

The stellar debris moves around the black hole for several orbits. Over time, the debris stretches due to the spread in its constituent orbital energies, and the debris head interacts with the tail near apocentre, leading to significant energy dissipation in shocks. The binding energy of the stellar debris is substantially reduced by a sequence of orbit crossings, causing the debris to circularize. From Figures 5 and 6, the stellar debris clearly circularizes in Models 1 and 2. However, circularization has proceeded much less rapidly in Model 3, as we see from Figure 7.

Panel (b1) shows the evolution of specific binding energy in Models 1-3. Since the specific binding energy has not reduced from  $\epsilon_*$  to  $\epsilon_c$  even at the end of these runs, the circularization process has not yet completed. Adopting a simple extrapolation from  $\epsilon_*$  to  $\epsilon_c$ , the circularization timescales can be estimated to be  $\sim 120P_*$  in Model 1,  $\sim 180P_*$  in Model 2, and  $\sim 2500P_*$  in Model 3, respectively. These extrapolated timescales indicate strongly varying per-orbit efficiencies of shock dissipation: if this efficiency were constant, then  $t_c \propto a^{3/2}$ . In fact, the circularization timescale behaves in an inverse manner. The prominently long circularization timescale of Model 3 shows this counterintuitive behavior. This declining dissipation efficiency at fixed  $\beta$  and decreasing  $e_*$  is likely because the relative velocity between the debris head and the debris tail at their self-intersection decreases as we go from Model 1 to Model 3. This is a general feature of eccentric TDEs at fixed  $\beta$ : low eccentricity produces self-intersections closer to apocentre, with lower relative velocities. This is also confirmed by the

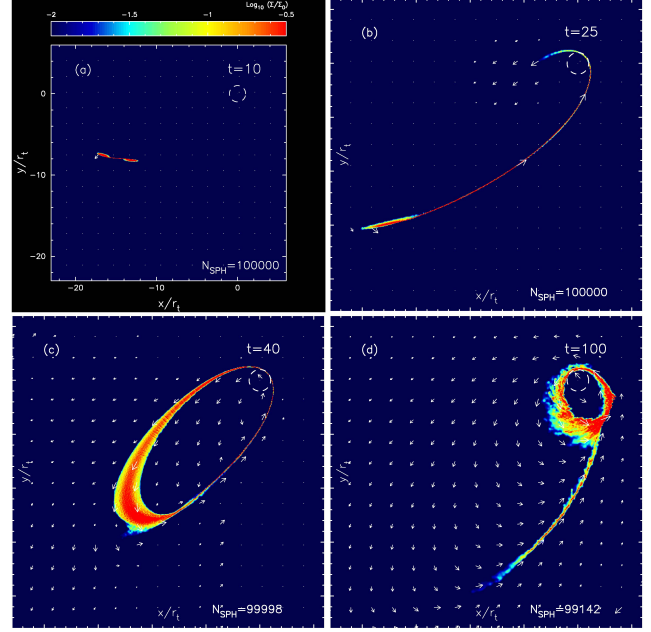


**Figure 5.** A sequence of snapshots of the tidal disruption process in Model 1 ( $a_* = 10 r_t$ ,  $e_* = 0.9$ ,  $\beta = 1$ ,  $\chi = 0.0$ , and  $i = 0^\circ$ ) in the radiatively efficient case. Panel (a) to (d) are shown in chronological order. All the panels show a surface density projected on the  $x$ - $y$  plane for  $0 \leq t \leq 100$ . The color bar shows the magnitude of the density in a logarithmic scale, where  $\Sigma_0 = 6.5 \times 10^6 \text{ g cm}^{-2}$  is the fiducial surface density (see equation 10). The black hole is set at the origin. The run time  $t$  is in units of  $P_*$  and is annotated at the top-right corner. The number of SPH particles are indicated at the bottom-right corner. The white small arrows and the dashed circle indicate the velocity field of the stellar debris and the tidal disruption radius, respectively.

difference between the orbital periods of most tightly and loosely bound gas, which shrinks as the orbital eccentricity decreases. These periods are given by (Hayasaki et al. 2013)

$$t_{\text{mtb}} = \frac{1}{2\sqrt{2}} \left[ \frac{1}{\beta(1-e_*)} \right]^{3/2} P_*, \quad (15)$$

$$t_{\text{mlb}} = \frac{1}{2\sqrt{2}} \left[ \frac{\beta(1-e_*)}{2} - q_*^{1/3} \right]^{-3/2} P_*, \quad (16)$$

where  $q_* = m_*/M_{\text{BH}}$ . Panel (b1) shows that the energy dissipation rate increases with orbital eccentricity for the case of  $\beta = 1$ . This implies that stellar debris should efficiently circularize in most standard, parabolic TDEs ( $\beta = 1$  and  $e_* = 1$ ) around non-spinning SMBHs.

### 3.2 Radiatively inefficient cooling cases

Next, we describe the results of our radiatively inefficient cooling simulations for Models 1-3. Figures 8-10 show a sequence of snapshots of debris surface density for Models 1-3, with the same figure formats as in Figure 5, but for the radiatively inefficient cooling simulations.

In Figure 8, the stellar debris moves away from the black hole following tidal disruption, as shown in panel (a), and is then stretched during pericentre return in panel (b). Near

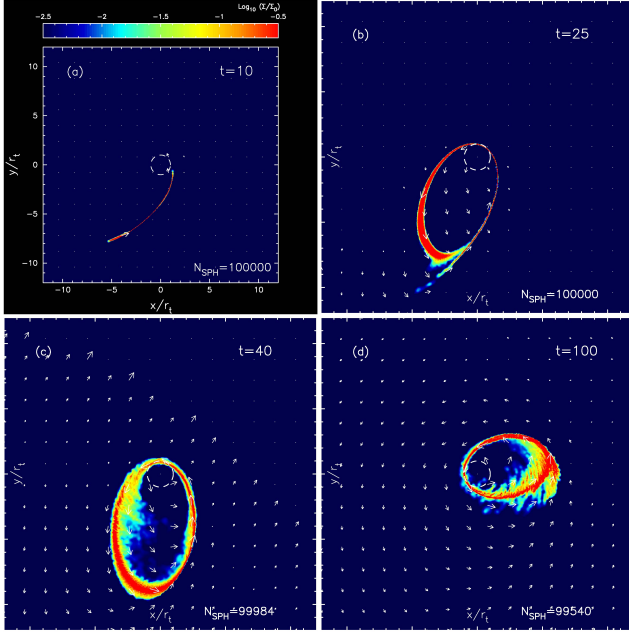


**Figure 6.** A sequence of snapshots of the tidal disruption process in Model 2 ( $a_* = 5 r_t$ ,  $e_* = 0.8$ ,  $\beta = 1$ ,  $\chi = 0.0$ , and  $i = 0^\circ$ ) in the radiatively efficient case. The figure formats are the same as Figure 5.

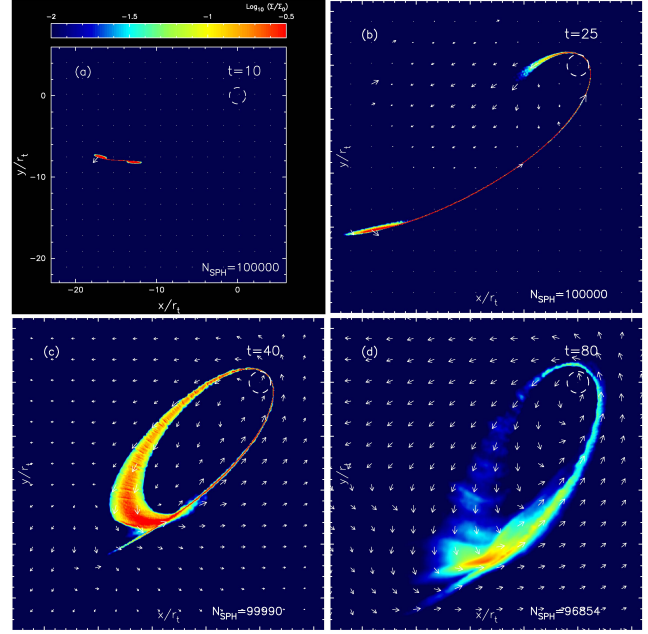


**Figure 8.** A sequence of snapshots of the tidal disruption process in Model 1 ( $a_* = 10 r_t$ ,  $e_* = 0.9$ ,  $\beta = 1$ ,  $\chi = 0.0$ , and  $i = 0^\circ$ ) in the radiatively inefficient case. The figure formats are the same as Figure 5, but for  $0 \leq t \leq 80$ .

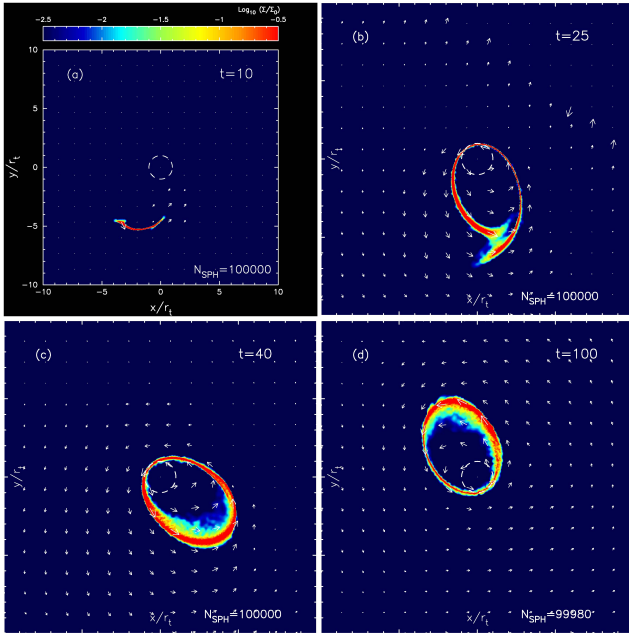


**Figure 7.** A sequence of snapshots of the tidal disruption process in Model 3 ( $a_* = 10 r_t/3$ ,  $e_* = 0.7$ ,  $\beta = 1$ ,  $\chi = 0.0$ , and  $i = 0^\circ$ ) in the radiatively efficient case. The figure formats are the same as Figure 5.

apocentre, the leading “head” of the debris significantly intersects with the trailing “tail,” as can be seen in panel (c). After several tens of orbits, the debris expands significantly, as the thermal energy increases from shock heating. This can be seen in panel (d).

There is a clear difference between Model 1 and Models

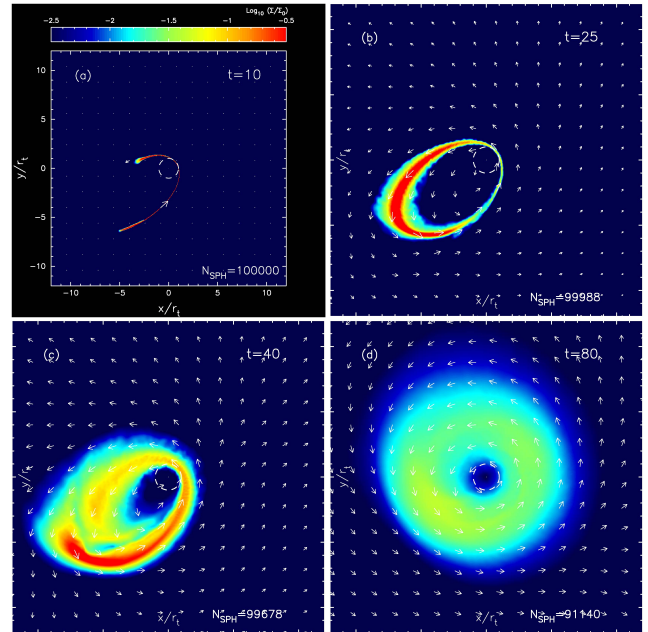


**Figure 9.** A sequence of snapshots of the tidal disruption process in Model 2 ( $a_* = 5 r_t$ ,  $e_* = 0.8$ ,  $\beta = 1$ ,  $\chi = 0.0$ , and  $i = 0^\circ$ ) in the radiatively inefficient limit. The figure formats are the same as Figure 5, but for  $0 \leq t \leq 80$ .

2-3. While no accretion disk forms by the end of simulation in Model 1, an accretion disk clearly forms and viscously evolves in Models 2 and 3. This viscous evolution can be understood as follows: the viscous timescale for an  $\alpha$ -viscosity disk is given by



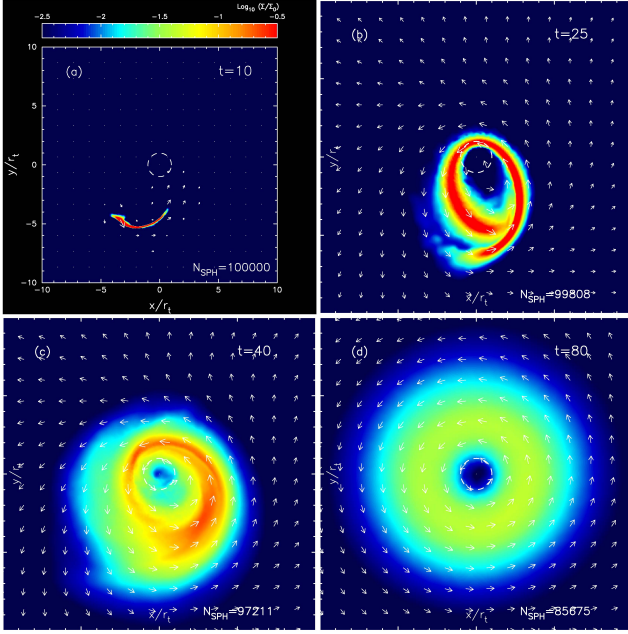


**Figure 10.** A sequence of snapshots of the tidal disruption process in Model 3 ( $a_* = 10/3 r_t$ ,  $e_* = 0.7$ ,  $\beta = 1$ ,  $\chi = 0.0$ , and  $i = 0^\circ$ ) in the radiatively inefficient limit. The figure formats are the same as Figure 5, but for  $0 \leq t \leq 80$ .

$$t_{\text{vis}} \sim \frac{r^2}{\nu} \sim \frac{5}{\pi} \left( \frac{0.1}{\alpha_{\text{SS}}} \right) \left( \frac{r}{r_t} \right)^{3/2} \left( \frac{H}{r} \right)^{-3/2} P_*. \quad (17)$$

The viscous timescale can be comparable to the debris orbital period because of the enhanced pressure and resultant geometrically thick structure ( $H/r \sim 1$ ) in the radiatively inefficient regime, meaning that rapid viscous redistribution of angular momentum and energy is possible. However, our simulations become significantly less reliable at late times, after formation of the accretion disk, due to the lack of radiation pressure and magneto-hydrodynamics in our code. We present these late-time results for completeness, but emphasize that our simulations are primarily designed only to simulate the circularization process itself.

Figure 4 shows evolution of the specific angular momentum and specific energy in Models 1-9, which are averaged per SPH particle. Panels (d1)-(d3) show the evolution of the specific energy in Models 1-9. The specific energy increases with time, in stark contrast with the radiatively efficient case. Preferential accretion of highly bound SPH particles increases, over time, the mean specific energy of non-accreted SPH particles. Panels (c1)-(c3) show the evolution of specific angular momentum averaged over all remaining SPH particles. This also increases with time because of preferential accretion of the lowest angular momentum SPH particles.

As a check on our radiative efficiency assumptions, we compare the photon diffusion timescale with the timescale for energy dissipation by shock heating. We estimate this latter timescale using the difference between the orbital periods of the most tightly and loosely bound gas, which are given by equations (15) and (16), respectively. These timescales are shown for each model in Table 1. Model 1 has the longest energy input timescale among all models, on the order of  $10^5$  s. From Figure 11, the surface density of the stellar debris and its scale height are estimated to be  $\Sigma/\Sigma_0 \sim 10^{-0.8}$

and  $H/r_t \sim 1$  for Model 1. Substituting into equation (8), the photon diffusion timescale is  $\sim 10^7$  s, clearly longer than the shock heating timescale. It is therefore clear that eccentric TDEs operate in the radiatively inefficient regime, although as we have argued above, the parabolic case is more ambiguous.

### 3.3 Comparison to pseudo-Newtonian potential simulation

In this section, we compare our SPH simulation with 2PN corrections to our SPH simulation with a pseudo-Newtonian potential. The PN simulation of Model 10, whose parameters can be seen in Table 1, was performed for the purpose of comparing with the pseudo-Newtonian simulation model. In Model 10, we used the same initial condition as that of Model 2a in our previous paper (Hayasaki et al. 2013). The initial position and velocity are set by

$$\begin{aligned} \mathbf{r}_0 &= (r_0 \cos \phi, r_0 \sin \phi, 0), \\ \mathbf{v}_0 &= (\dot{r}(r_0) \cos \phi_0 - r_0 \dot{\phi}(\phi_0) \sin \phi_0, \dot{r}(r_0) \sin \phi_0 \\ &\quad + r_0 \dot{\phi}(\phi_0) \cos \phi_0, 0), \end{aligned}$$

where  $r_0 = a_*(1 - e_*)$  and  $\phi_0 = -0.2\pi$  are adopted. Here, the radial velocity  $\dot{r}$  and angular velocity  $\dot{\phi}$  are given by energy conservation and angular momentum conservation as

$$\begin{aligned} \dot{r} &= \sqrt{2(\epsilon_{\text{pseudo}} - U(r)) - \frac{l_{\text{pseudo}}^2}{r^2}}, \\ \dot{\phi} &= \frac{l_{\text{pseudo}}}{r^2}, \end{aligned}$$

where  $\epsilon_{\text{pseudo}}$  and  $l_{\text{pseudo}}$  are the specific energy and the specific angular momentum for bound orbits, the pseudo-Newtonian potential (Wegg 2012), respectively. They are written by

$$\begin{aligned} U(r) &= -\frac{GM_{\text{BH}}}{r} \left[ c_1 + \frac{1 - c_1}{1 - c_2(r_s/2r)} + c_3 \frac{r_s}{2r} \right], \\ \epsilon_{\text{pseudo}} &= \frac{(r_p/r_a)^2 U(r_p) - U(r_a)}{(r_p/r_a)^2 - 1}, \\ l_{\text{pseudo}} &= \sqrt{2r_p^2(\epsilon - U(r_p))} = \sqrt{2r_a^2(\epsilon - U(r_a))}, \end{aligned} \quad (18)$$

where  $r_p = a_*(1 - e_*)$  and  $r_a = a_*(1 + e_*)$  are the pericenter distance and the apocenter distance, respectively, and we adopt that  $c_1 = (-4/3)(2 + \sqrt{6})$ ,  $c_2 = (4\sqrt{6} - 9)$ , and  $c_3 = (-4/3)(2\sqrt{6} - 3)$ . The initial position and velocity vector for Model 10 are seen in Table 2.

Figure 12 shows the evolution of specific binding energy and angular momentum. In panel (a), the blue solid, red solid, and black dashed lines show the specific angular momenta of Model 10, our pseudo-Newtonian simulation model, and  $l_{\text{pseudo}}$  respectively. From the panel, we note that the angular momentum is conserved for the pseudo-Newtonian case, while it is shifted at the  $\sim 20\%$  level from the Newtonian specific angular momentum and at the 3% level even from the pseudo-Newtonian case. In panel (b), the blue solid, red solid, and black dashed lines show the specific binding energies of Model 10, our pseudo-Newtonian simulation model, and  $\epsilon_{\text{pseudo}}$  respectively. From the panel, the specific binding energy first agrees well with that of test particle, but substantially reduces due to debris circularization, and eventually saturates at  $\sim 7P_*$  in the pseudo-

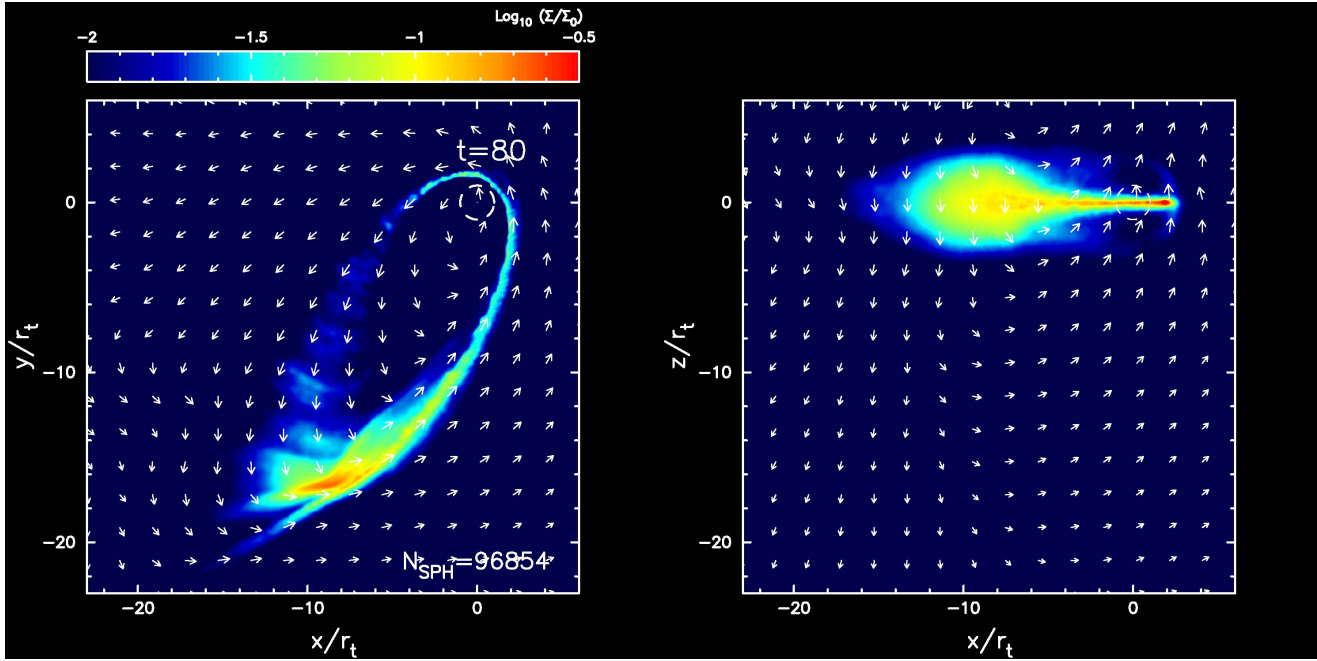


**Figure 11.** Density map for Model 1 ( $a_* = 10 r_t$ ,  $e_* = 0.9$ ,  $\beta = 1$ ,  $\chi = 0.0$ , and  $i = 0^\circ$ ) in the radiatively inefficient cooling limit. Each panel shows surface densities projected on  $x$ - $y$  plane (left panel) and on  $x$ - $z$  plane (right panel) at  $t = 80$ . The figure formats are the same as Figure 5.

Newtonian case. This is because there is less shock energy dissipation required for accretion disk formation (see Figure 12 of Hayasaki et al. 2013). On the other hand, the specific binding energy of Model 10 is slightly shifted from that of test particle:  $\epsilon_{\text{pseudo}} = \epsilon_* = -0.5\epsilon_t$ , with some small oscillation.

The errors of Model 10 in those two panels are attributed to the intrinsic error of PN corrections. In this comparison, the error of angular momentum is substantially larger than that of binding energy. This trend is different from our other simulation results and test particle simulations (see Table 2). This is probably attributed to the higher  $\beta$  value of Model 10.

Debris circularization is significantly more efficient in the pseudo-Newtonian simulation. This is because the precession rate is larger than that of Model 10. Since the pericentre velocity of the debris in these models is a significant fraction of the speed of light, the PN approximation should break down. Thus, our simple PN approaches to relativistic effects should not be applicable for such a high  $\beta$  simulation as  $\beta = 5$ .

Bonnerot et al. (2015) have recently performed similar SPH simulations for accretion disk formation around a non-spinning SMBH. Some of their simulations have used the same simulation parameters and setup as (Hayasaki et al. 2013) but for a recently derived pseudo-Newtonian potential, isothermal equation of state, and 500K SPH particles. We have compared the black line of their Figure 3 (Model RI5e.8) with two lines of panel (b) of Figure 12. The specific energy evolution of their model, while similar to our older pseudo-Newtonian simulation, differs significantly from our PN Model 10. Specifically, they see more rapid circularization. This could be due to the somewhat different equations of state employed (isothermal vs polytropic) or our

lower particle resolution, but is most likely due to differences in the gravitational potential employed. While both potentials accurately account for apsidal precession around Schwarzschild SMBHs in  $\beta = 1$  and  $\beta = 2$  events, our PN approach begins to break down for Model 10's  $\beta = 5$ , underestimating the true precession rate and therefore generating an artificially weak (and delayed) stream self-intersection. We hope to perform more detailed comparisons in future work.

For  $\beta = 1$  and  $e = 0.8$ , our radiatively efficient simulation for Model 2 is the same as their Model RI1e.8, but for the pseudo-Newtonian potential, isothermal equation of state, and 500K SPH particles. We have compared the red dashed line of their Figure 10 (Model RI1e.8) with the blue line of panel (b1) of our Figure 3 at  $t \sim 90$ , which corresponds to the end of their simulation. The onset of the energy dissipation in their model is similar to ours, but their dissipated energy estimated at  $t \sim 90$  is  $\sim 25\%$  smaller than our dissipated energy. This could mainly originate from the low resolution of the simulation. We will discuss the numerical convergence problem in the next section.

### 3.4 Numerical convergence

In order to test the numerical convergence of our simulations, we have repeated Model 4 with 200K and 500K SPH particles (as opposed to our standard 100K SPH particles). Figure 13 shows the evolution of specific angular momentum and energy for Model 4 in both the radiatively efficient and inefficient cooling regimes. In panels (a)-(d), the red and black lines are the 200K and 100K cases, respectively. Note that the blue solid line of panel (b) shows normalized specific binding energy until  $t \approx 38$  for the 500K particles' simulation. The specific angular momentum of the higher resolution case is better-conserved, but both simulations are

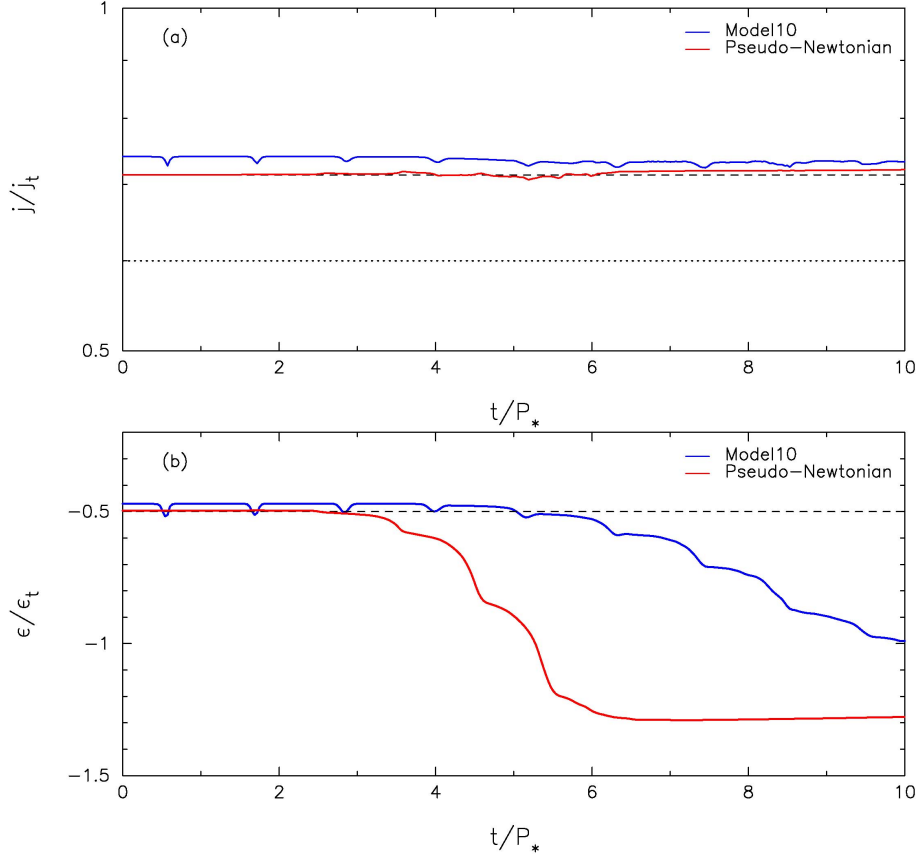


**Figure 12.** Evolution of the specific angular momentum and specific binding energy in Model 10 and our pseudo-Newtonian simulation model. These are averaged out per SPH particle. The specific binding energy and specific angular momentum are normalized by  $\epsilon_t = GM_{\text{BH}}/r_t$  and  $j_t = \sqrt{GM_{\text{BH}}r_t}$ , respectively. In panels (a), the blue and red solid lines denote the specific angular momentum of Model 10 and pseudo-Newtonian model, respectively. The dashed and dotted lines denote  $l_{\text{pseudo}}$  and the specific angular momentum of a test particle moving under the Newtonian potential,  $j_* = \sqrt{a_*(1 - e_*^2)}$ , respectively. In panel (b), the blue and red solid lines represent the specific binding energy of Model 10 and pseudo-Newtonian model, respectively. The dashed lines show  $\epsilon_{\text{pseudo}}$ , which approximately equals to the Newtonian specific binding energy of a test particle,  $\epsilon_* = -(1/2)\beta(1 - e_*)\epsilon_t$ .

well-converged at a less than 0.2% level for the radiatively efficient regime.

Because the angular momentum is conserved, the specific binding energy at the circularization radius is estimated to be  $\epsilon_c \approx 0.588$  for Model 4 from equation (5). The 200K simulation achieves complete circularization by the end of the simulation, but the 100K and 500K simulations do not. There is a  $\sim 17\%$  difference of the final energy distributions between 100K and 200K particles' simulations, and a  $\sim 14\%$  difference between the 100K and 500K simulations. This indicates that the late stages of debris circularization are not numerically converged in our radiatively efficient simulations with  $N_{\text{SPH}} = 100\text{K}$ . The 200K case is slightly more dissipative, by  $\sim 3\%$ , compared with 500K case, because the lower resolution makes the artificial viscosity larger. Thus, the 500K case is better converged than 200K case.

An equivalent convergence test on Model 4 with a radiatively inefficient (adiabatic) equation of state finds a smaller,  $\approx 10\%$ , difference between the final energy distributions of the 100K and 200K cases (see panel (d) of Figure 13). Importantly, the radiatively inefficient runs appear much more closely converged through the end of the circularization process, and they only diverge from each other as the thick torus

begins to viscously accrete (which is not the main focus of this work). Although our radiatively inefficient simulations appear to have converged in their description of debris circularization, our radiatively efficient runs are underestimating the true efficiency of debris circularization due to resolution effects. This is a topic we will examine more clearly in future work.

#### 4 STELLAR TIDAL DISRUPTION BY A SPINNING BLACK HOLE

Finally, we investigate the tidal disruption of a star by a spinning SMBH. First, we see how black hole spin affects coplanar debris circularization through simulations of Models 4-6. Second, we examine Lense-Thirring precession of stellar debris during the tidal disruption process, in Models 7-9. We have used Model 4 specifically to check our results for numerical convergence, by running two higher resolution versions (one for each equation of state) with 200K SPH particles. We find that Model 4 is well-converged for the radiatively inefficient regime during the period of debris circularization, but in the radiatively efficient regime, our

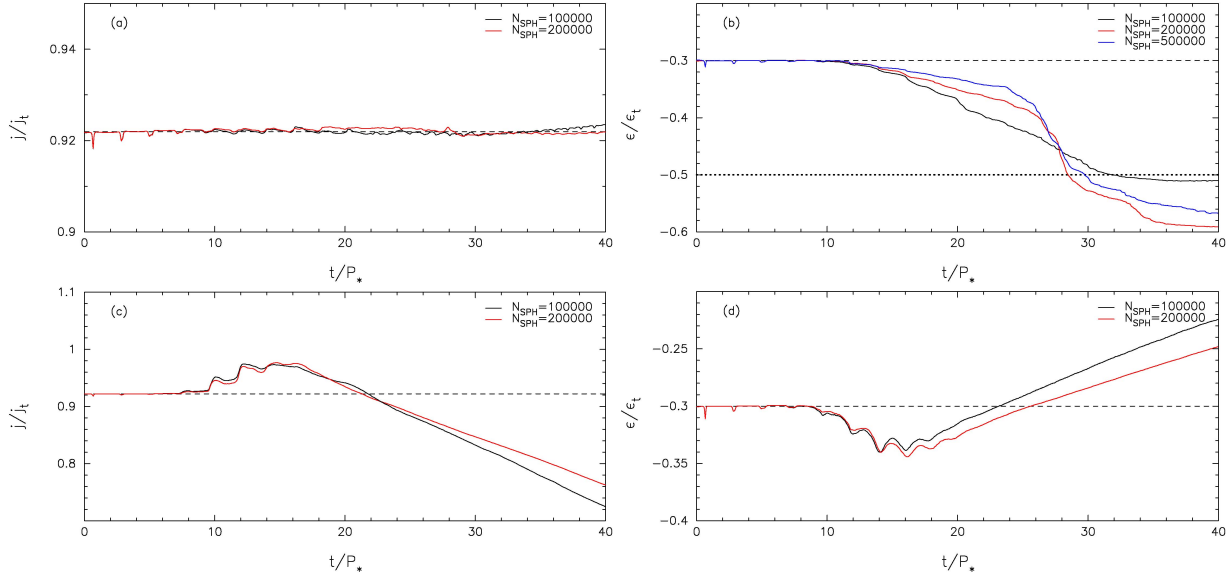


**Figure 13.** Evolution of the specific angular momentum and energy for Model 4 with  $N_{\text{SPH}} = 200\text{K}$  (as opposed to our standard  $100\text{K}$  SPH particles). These are averaged out per SPH particle. Panels (a) and (b) are for the radiatively efficient cooling simulation, whereas panels (c) and (d) are for the radiatively inefficient cooling simulation. In panels (a) and (c), the black and red solid lines denote the specific angular momentum normalized by  $j_t = \sqrt{GM_{\text{BH}}t}$  for  $100\text{K}$  and  $200\text{K}$  SPH particles' simulations, respectively. In panels (b) and (c), the black and red solid lines represent the specific binding energy normalized by  $\epsilon_t = GM_{\text{BH}}/r_t$  for  $100\text{K}$  and  $200\text{K}$  SPH particles' simulations, respectively. In panel (b), the blue solid line shows the evolution of the normalized specific energy of the  $N_{\text{SPH}} = 500\text{K}$  simulation for Model 4. All other figure formats are the same as Figure 3.

lower-resolution fiducial runs may be underestimating the efficiency of shock dissipation (see panel (b) of Figure 13).

#### 4.1 Effect of black hole spin on debris circularization

First, we examine the circularization of stellar debris in the radiatively efficient cooling case for Models 4-6, in which the vector of black hole spin is aligned with z-axis. We note, from panel (b2) of Figure 3, that the energy dissipation rate of Model 6 is highest among these three models. This shows that the enhanced apsidal precession of retrograde black hole spin makes debris circularization more efficient than in the non-spinning black hole case, whereas prograde black hole spin substantially delays debris circularization by decreasing the apsidal precession rate (Merritt et al. 2010). Debris circularization progresses rapidly but saturates at a specific energy slightly less than  $\epsilon_t$  in Models 4 and 6 without reaching  $\epsilon_c$ , at which point debris circularization would be completed. This incomplete circularization is because relative velocities between debris head and tail at self-intersections (near apocentre) are too low to produce significant shock dissipation. This could originate from the low resolution of the simulation (see section 3.4).

We also simulate coplanar circularization processes, in Models 4-5, for a tidally disrupted star around a spinning SMBH in the radiatively inefficient cooling limit. From panel (d2), we see that the specific energy increases with time after  $t = 10$ . As in Models 1-3, this is because the most tightly bound gas is preferentially accreted by the black hole, increasing the average specific energy of remaining disk matter. The circularized accretion torus extends to much larger radii than in the radiatively efficient case, as some of the

gas spreads to more loosely bound circular orbits due to hydrodynamic effects. Specific angular momentum also increases with time after  $t = 10$ , again because of preferential accretion.

The main difference between the different cooling regimes is clear from comparing Figure 14 and Figure 15, which show a sequence of snapshots for Model 5 in the radiatively efficient and inefficient cooling cases, respectively. These figures have the same formats as Figure 5, with each panel in chronological order, from panel (a) to (l). Increased thermal energy from shock heating causes the debris temperature to rise significantly at early times in the radiatively inefficient case, which produces a geometrically thick accretion disk at late times. This is in sharp contrast to the geometrically thin gas structure produced in the radiatively efficient case of Figure 14. We have also performed radiatively inefficient simulations of Models 7-9. These differ from their radiatively efficient counterparts in several qualitative ways, which we discuss next.

The effect of the inclination angle between the black hole spin vector and the disk angular momentum vector on debris circularization can be seen in panel (b3). When the black hole rotates retrogradely as in Models 7 and 8, the circularization timescale is about  $\sim 30P_*$ . This is longer than the circularization timescale  $\sim 20P_*$  of the coplanar case (Model 6) as can be seen from the red line in panel (b2). However, the specific binding energy saturates at  $\sim \epsilon_c$ , which is lower value than that of Model 6. Also, Models 7 and 8 periodically alternate between rapid energy dissipation followed by energy conservation, for  $14 \lesssim t \lesssim 40$ . This is because the stellar debris undergoes both relativistic apsidal and nodal precession (Stone et al. 2015). The stellar debris dissipates orbital energy in shocks due to apsidal precession,

but since the debris undergoes nodal precession with each pericenter passage, streams that would exactly self-intersect in the coplanar case miss each other by a small amount. This is the origin of the saturation phase of specific energy evolution. Figure 16 shows a sequence of snapshots of the tidal disruption process in Model 7 in the radiatively efficient limit. Each panel shows surface densities projected on the  $x$ - $y$  plane (left panel) and on the  $y$ - $z$  plane (right panel) for  $0 \leq t \leq 40$ . After tidal disruption, the debris in this run circularizes into a thin ring-like structure that slowly rotates around the  $x$ -axis due to Lense-Thirring precession. As seen in the panels (c)-(e), the multiple ring-like structures formed by the cumulative effect of nodal precession enable intersections with large relative velocity even at late times (Stone et al. 2015). This enhances both the energy dissipation rate and the total amount of dissipated energy above those of the coplanar case.

#### 4.2 Nodal precession caused by the Lense-Thirring effect

Figure 17 shows the evolution of a tilt angle  $\theta_{\text{tilt}}$  and precession angle  $\theta_{\text{prec}}$  (equivalent to the nodal angle in standard orbital elements) for Models 7-9. These angles are defined as (Nelson & Papaloizou 2000; Fragile & Anninos 2005)

$$\theta_{\text{tilt}} = \arccos \left[ \frac{\mathbf{J}_{\text{BH}} \cdot \mathbf{J}_{\text{d}}}{|\mathbf{J}_{\text{BH}}| |\mathbf{J}_{\text{d}}|} \right] \quad (19)$$

$$\theta_{\text{prec}} = \arccos \left[ \frac{\mathbf{J}_{\text{BH}} \times \mathbf{J}_{\text{d}}}{|\mathbf{J}_{\text{BH}}| |\mathbf{J}_{\text{d}}|} \cdot \hat{\mathbf{y}} \right], \quad (20)$$

where  $\mathbf{J}_{\text{d}}$ ,  $\mathbf{J}_{\text{BH}}$  and  $\hat{\mathbf{y}}$  are the angular momentum vector of the stellar debris, black hole spin vector, and the unit vector of the  $y$ -axis, respectively. Here, we set  $\mathbf{J}_{\text{BH}} = (1, 0, 0)$  for Model 7,  $\mathbf{J}_{\text{BH}} = (1/\sqrt{2}, 0, 1/\sqrt{2})$  for Model 8, and  $\mathbf{J}_{\text{BH}} = (-1/\sqrt{2}, 0, -1/\sqrt{2})$  for Model 9.

We see from this figure that the tilt angle remains constant, but the precession angle increases with time in all three models. This is in rough agreement with our expectations for nodal precession caused by frame dragging torques. Let us focus on the radiatively efficient case of Model 7 as a concrete example. In the early stages of debris circularization, the precession angle per orbital period in our simulations is roughly  $\sim 0.01\pi$ . This is in good agreement with the theoretically expected (to lowest PN order) change per orbit of the nodal angle for a test particle orbiting around a spinning black hole,

$$\frac{\theta_{\text{LT},*}}{2\pi} = \frac{2\chi}{c^3} \left[ \frac{GM_{\text{bh}}}{r_{\text{p}}(1+e_*)} \right]^{3/2} = \frac{\chi}{\sqrt{2}} \left( \frac{r_{\text{t}}}{r_{\text{S}}} \right)^{-3/2} \left( \frac{\beta}{1+e_*} \right)^{3/2}, \quad (21)$$

where  $r_{\text{p}} = a_*(1 - e_*)$  is the pericentre distance. This is given by equations (6b) and (8) of Merritt et al. (2010), using equation (4) of this paper, which shows the changes per orbit of the nodal angle due to frame dragging torques.

In the late stages of debris circularization, stellar debris has begun to form an accretion disk. In this phase, the precession angle per orbit grows to  $\sim 0.02\pi$ . This is in good agreement with the the change per orbit of the nodal angle of an accretion disk, which is given by

$$\frac{\theta_{\text{LT,disk}}}{2\pi} = \frac{\chi}{\sqrt{2}} \left( \frac{r_{\text{t}}}{r_{\text{S}}} \right)^{-3/2} \left( \frac{r_{\text{i}}}{r_{\text{t}}} \right)^{-3}$$

$$\times \left( \frac{2\zeta - 5}{2\zeta + 1} \right) \frac{1 - (r_{\text{i}}/r_{\text{o}})^{\zeta+1/2}}{1 - (r_{\text{i}}/r_{\text{o}})^{\zeta-5/2}}, \quad (22)$$

where  $r_{\text{i}}$ ,  $r_{\text{o}}$ ,  $\zeta$  are the inner radius, outer radius, and power law index of the disk surface density, respectively. We have approximated  $(\theta_{\text{LT,disk}}/2\pi) = P_*/t_{\text{LT,disk}}$ , where  $t_{\text{LT,disk}}$  is the precession timescale given by equation (3) of Stone & Loeb (2012a).

The local Lense-Thirring precession timescale is given by

$$\tau_{\text{LT}} = \frac{2\pi}{\Omega_{\text{LT}}} = 2\pi \left( \frac{2}{\chi} \right) \left( \frac{r_{\text{S}}}{c} \right) \left( \frac{r}{r_{\text{S}}} \right)^3, \quad (23)$$

where  $\Omega_{\text{LT}} = 2\chi(GM)^2/(rc)^3$  (Bardeen & Petterson 1975). The vertical viscosity timescale is

$$\tau_{\text{vis}} = \frac{2\sqrt{2}}{3} \left( \frac{1}{\eta\alpha_{\text{SS}}} \right) \left( \frac{r_{\text{S}}}{c} \right) \left( \frac{r}{r_{\text{S}}} \right)^{3/2} \left( \frac{H}{r} \right)^{-2}, \quad (24)$$

where  $\eta = 2(1 + 7\alpha_{\text{SS}}^2)/(\alpha_{\text{SS}}^2(4 + \alpha_{\text{SS}}))$  is the ratio of the vertical viscosity to horizontal viscosity (Ogilvie 1999; Lodato & Price 2010). For  $\alpha_{\text{SS}} \ll 1$ ,  $\eta \approx 1/2\alpha_{\text{SS}}^2$  (Papaloizou & Pringle 1983). If the local precession timescale is shorter than the vertical viscous timescale, the disc is not warped and precesses as a rigid body. This condition is given by

$$\frac{r}{r_{\text{S}}} \gtrsim \left( \frac{\sqrt{2}}{3\pi} \right)^{2/3} \left( \frac{H}{r} \right)^{-4/3} \chi^{2/3} \alpha_{\text{SS}}^{2/3} \quad (25)$$

for  $\alpha_{\text{SS}} \ll 1$ . For typical parameters of the geometrically thick disc:  $H/r \sim 1$ ,  $\alpha_{\text{SS}} = 0.1$ , and  $\chi = 0.9$ , the condition gives  $r \gtrsim 6 \times 10^{-2} r_{\text{S}}$ . We obtain the condition  $r \gtrsim r_{\text{t}}$  for the geometrically thin disc case  $H/r \sim 0.01$ . While the disc rigidly precesses in the radiatively inefficient cases, it is unlikely to in the efficient cooling cases at the current low resolution simulation.

The roughly rigid body precession seen in our efficient cooling simulations is likely an artifact of the narrow ring-like configuration that is preserved here because of the short simulation runtime. If these simulations were run for longer than a viscous time, the spreading gas rings would likely develop Bardeen-Petterson warps (Bardeen & Petterson 1975). More realistically, however, the disc viscosity should be much less than that of our simulations, because the artificial viscosity used here would be overestimated by the low resolution simulations. Therefore, the disc would be warmer and geometrically thicker, causing the disc to be closer to the wavelike regime of warp propagation. Even for large,  $\sim 10^8$  solar mass SMBHs where the gas streams and an eccentric disc may initially be radiatively efficient (as we argue), a fully circularized disc will likely be radiatively inefficient. In most TDEs, therefore, the disc can rigidly precess, because the Lense-Thirring timescale is longer than the timescale the warps propagate as a wave. Franchini et al. (2016) have recently shown that the internal dissipation in the disc can quench the rigid-body precession while it remains geometrically thick, although typically after the accumulation of several precession periods. Our simulations do not run long enough to observe such an effect.

There is a remarkable difference between Models 7-9 in the radiatively efficient case, and an even starker difference between radiatively efficient and inefficient simulations of these models. In Figure 17, the dashed lines show the evolution of nodal angles for the geometrically thick disks of our



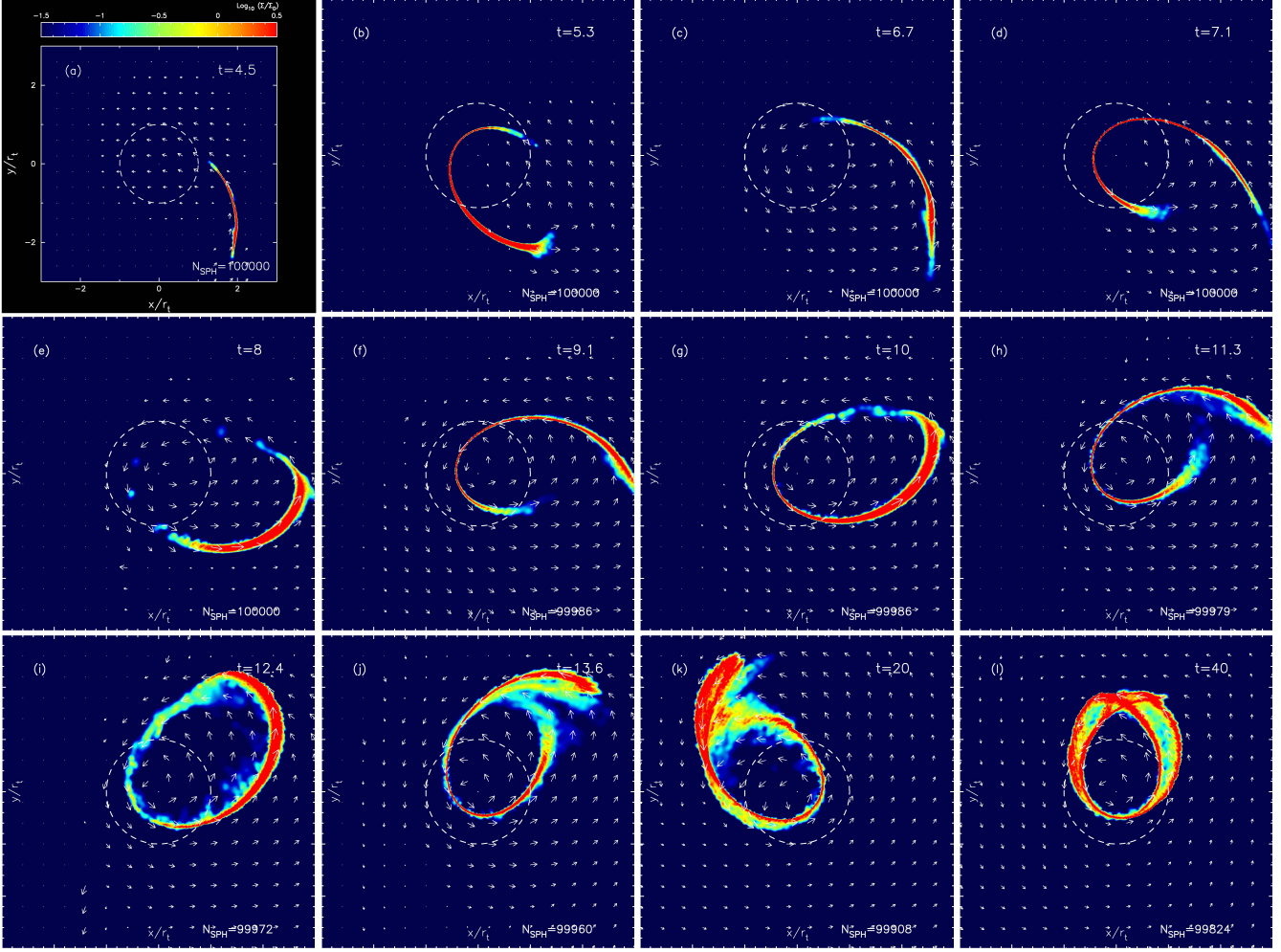


**Figure 14.** A sequence of snapshots of the tidal disruption process in Model 5 ( $a_* = 5/3$ ,  $e_* = 0.7$ ,  $\beta = 2$ ,  $\chi = 0.9$ , and  $i = 0^\circ$ ) in the radiatively efficient regime. They run from panel (a) to panel (l) in chronological order. Each panel shows surface densities projected on the  $x$ - $y$  plane over two orders of magnitude in a logarithmic scale for  $0 \leq t \leq 40$  (see also color bar), where  $t$  is in units of  $P_*$ . The black hole is set at the origin. The run time is annotated at the top-right corner, while the number of SPH particles are indicated at the bottom-right corner. The dashed circle indicates the tidal disruption radius.

radiatively inefficient scenarios, while solid lines show this in the radiatively efficient ones. In the radiatively efficient case, there are two stages in the nodal angle evolution. In the early stage until  $t \sim 12P_*$ , all the nodal angle curves are overlapping as theoretically expected. In the later stage, they split in three. These differences between Models 7-9 are explained by their somewhat different values of  $r_i$  and  $r_o$ , which are caused by the difference of formation speed of the debris rings. As shown in panel (c2) of Figure 3, the debris ring of Model 8 forms more quickly than that of Model 7, which forms more quickly than that of Model 9.

The green solid line of Figure 17 denotes the evolution of the nodal angle of the radiatively efficient  $N_{\text{SPH}} = 500\text{K}$  simulation for Model 7. The comparison between the 100K and 500K cases shows that the precession rate of the 500K case is smaller than the 100K case in the latter evolution stage, because the inner edge radius of the disc is larger than the 100K case by the smaller artificial viscosity owing to the smaller smoothing length of the 500K case (i.e. higher

resolution). It is seen from equation (22) that the larger inner edge radius makes the nodal precession slower.

On the other hand, there is only one stage in the nodal angle evolution in the radiatively inefficient limit. Since the geometrically thick disks of Models 7-9 have almost identical surface density profiles in the late stage, all the curves overlap for  $0 \leq t \leq 40$ . If we adopt representative values for these realistic disks, e.g.  $r_i = 1.5r_t$ ,  $r_o = 4.5r_t$ , and  $\zeta = 2.0$  from Figure 18, the precession timescale is estimated to be  $t_{\text{LT,disk}} \sim 2 \times 10^3 P_*$ . This implies that the nodal angles of radiatively inefficient disks increase slowly, and at rates decreasing with time.

After debris circularization, the accretion disk will viscously evolve and accrete onto the black hole. In the efficient cooling case,  $t_{\text{vis}}$  is of the order of  $10^3 P_*$ , as  $H/r \sim 0.01$ . Since the viscous timescale is clearly longer than the precession timescale,  $\lesssim 10^2 P_*$ , the disk will rapidly precess around the black hole spin axis as the material accretes onto the black hole; this could potentially be imprinted on the observed light curve. In contrast,  $t_{\text{vis}}$  is of the order of  $P_*$  in

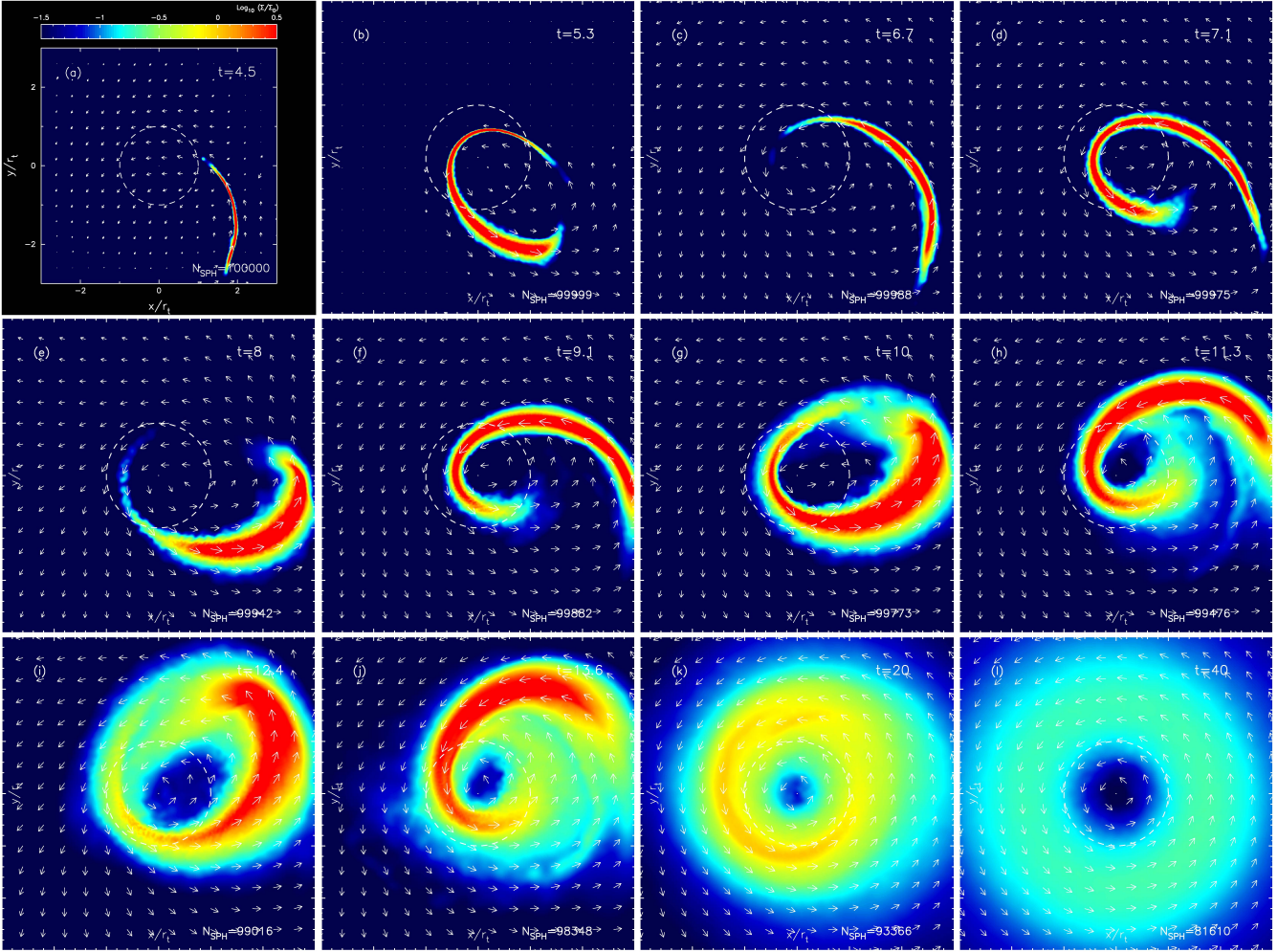


**Figure 15.** A sequence of snapshots of the tidal disruption process in Model 5 ( $a_* = 5/3$ ,  $e_* = 0.7$ ,  $\beta = 2$ ,  $\chi = 0.9$ , and  $i = 0^\circ$ ) in the radiatively inefficient limit. They run from panel (a) to panel (l) in chronological order. The figure format is the same as Figure 14.

the inefficient cooling case, where  $H/r \sim 1$  is adopted. The viscous timescale is therefore much shorter than the precession timescale  $\sim 10^3 P_*$ . In this regime, which is much more realistic for circularized disks in both eccentric and parabolic TDEs, most of the disk mass will drain onto the SMBH before it can significantly precess. In eccentric TDEs, this makes it unlikely that evidence for spin-induced precession can be found in the observed light curve. In parabolic TDEs, the disk is continuously replenished with new matter, so that unlike the eccentric TDE regime, disk precession may be observable.

## 5 SUMMARY & DISCUSSION

We have performed numerical simulations of circularization and subsequent accretion disk formation during the tidal disruption of stars on bound orbits around spinning and non-spinning SMBHs. We have approximated relativistic effects with simple Post-Newtonian corrections up to 2PN, including the lowest order spin terms (1.5PN). We have considered relatively low orbital eccentricity ( $e = 0.7 - 0.9$ ) with modest penetration factors  $\beta = 1 - 2$ . We have found that debris

circularization depends crucially on the efficiency of the radiative cooling, and therefore simulated our nine models in two limiting regimes: radiatively efficient, and radiatively inefficient. Our main conclusions are as follows:

(i) There are two stages in debris circularization if radiative cooling is inefficient: In the early stage, the stellar debris, stretched by tidal disruption, orbits and forms a geometrically thick ring-like structure around the black hole due to shock heating caused by orbital self-intersections induced by relativistic precession. In the late stage, the ring-like structure rapidly spreads via viscous diffusion, forming a geometrically thick accretion disk. In contrast, if radiative cooling is efficient, the stellar debris circularizes into a geometrically thin ring-like structure.

(ii) In relatively low eccentricity tidal disruptions, the stellar debris is clearly optically thick and its photon diffusion timescale is longer than the shock heating timescale, so stellar debris will circularize as in our radiatively inefficient cooling simulations. However, in a parabolic tidal disruption for  $M_{\text{BH}} \gtrsim 2 \times 10^6 M_\odot$ , our radiatively efficient simulations may be more relevant, because the photon diffusion timescale can be shorter than the fallback timescale.

(iii) In the radiatively efficient regime, debris circularizes

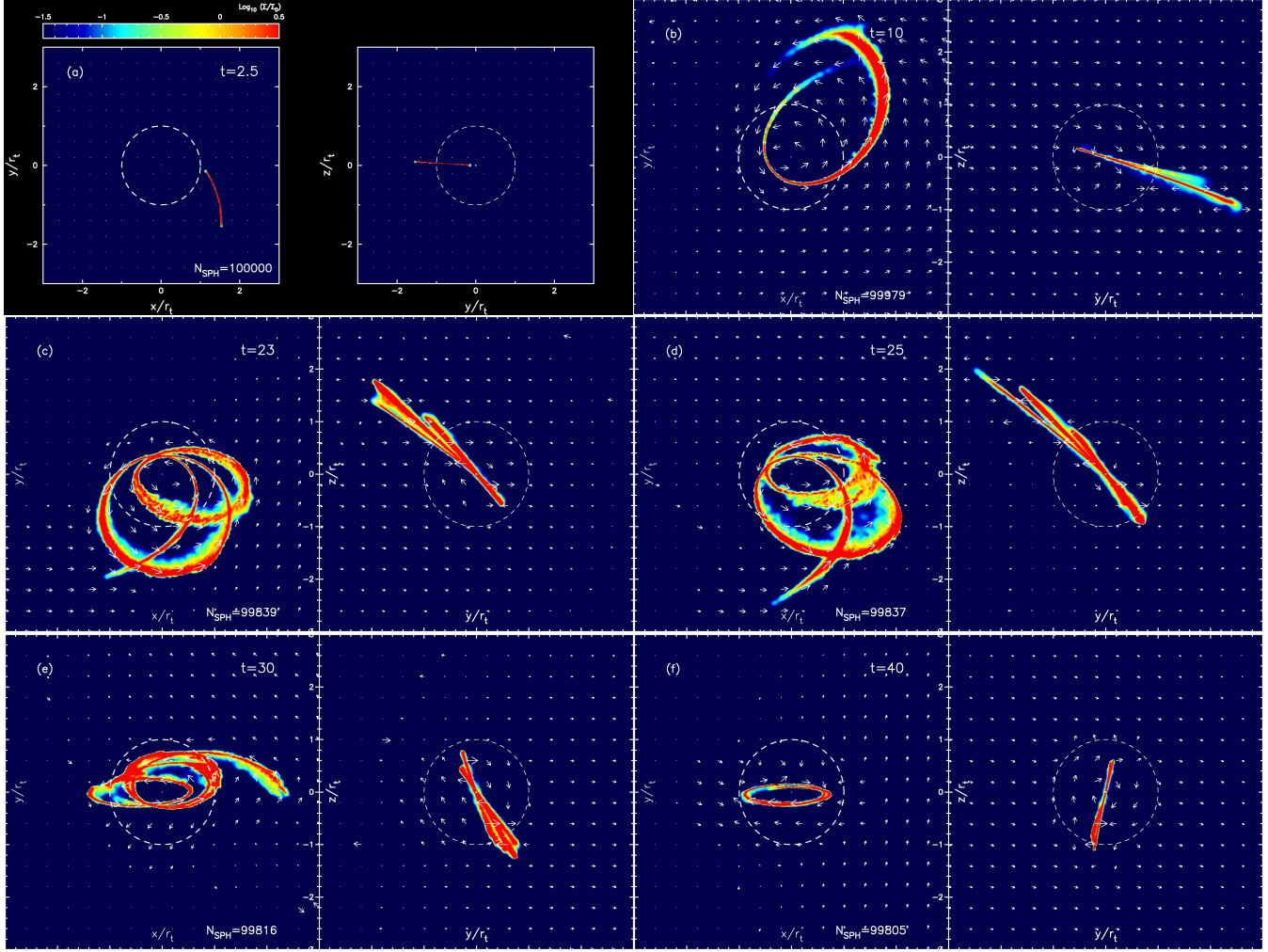


**Figure 16.** A sequence of snapshots of the tidal disruption process in Model 7 ( $a_* = 5/3$ ,  $e_* = 0.7$ ,  $\beta = 2$ ,  $\chi = -0.9$ , and  $i = 90^\circ$ ) in the radiatively efficient case. Each panel shows surface densities projected on  $x$ - $y$  plane (left panel) and on  $y$ - $z$  plane (right panel) for  $0 \leq t \leq 40$ . The other figure formats are the same as Figure 5.

more quickly for retrograde spins than for no spin, and more quickly for no spin than for prograde spins. This is because retrograde spin increases the apsidal shift per orbit, while prograde spin decreases it. Increased apsidal precession both reduces the time it takes for the debris head to catch its tail (increasing circularization rates for eccentric TDEs) and increases the relative velocity at the stream self-intersection point (increasing circularization rates for both eccentric and parabolic TDEs). This spin dependence is largely absent from the radiatively inefficient regime, where the increased stream thickness due to heating dominates more subtle GR effects. As discussed in section 3.4, our radiatively inefficient simulations appear numerically well-converged during the period of debris circularization, but the radiatively efficient simulations are underestimating the efficiency of shock dissipation in 100K particles' simulations.

(iv) When the the black hole spin axis is initially misaligned with the debris angular momentum vector, the circularized debris ring or disk precesses due to Lense-Thirring torque. While the tilt angles remains constant during debris circularization in both the radiatively inefficient and efficient cooling cases, the nodal precession angles vary with

time, indicating approximately solid-body precession. While nodal angles in both cases evolve in the same manner prior to significant energy dissipation in shocks, they evolve much more slowly in the radiatively inefficient regime during subsequent dissipative circularization, because the debris forms a geometrically thick accretion disk with much larger radial extent.

(v) In the radiatively efficient regime, debris circularization is significantly impeded by misaligned SMBH spin. Despite this retarding effect, however, it increases the total energy dissipated during debris circularization by the end of our simulations, although it is unlikely that the radiatively efficient cooling regime applies at late times, once debris is mostly circularized. Nodal precession of cool, thin debris streams may result in significantly reduced shock dissipation at self-intersection points, as the streams can miss each other completely, or suffer only a grazing collision.

Expanding on conclusion (v), we discuss how applicable these simulations of eccentric TDEs are to the presumably more common parabolic TDE scenario. The dynamics of stream self-intersections are very similar: as implied by



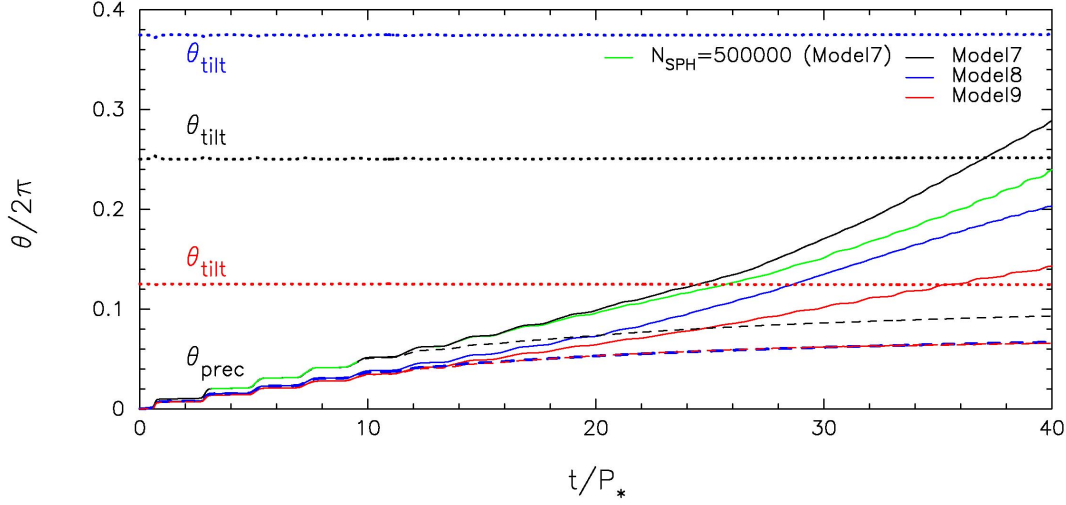


**Figure 17.** Evolution of the tilt and nodal angles for Models 7-9 in both the radiatively efficient and inefficient cooling cases. The tilt angle  $\theta_{\text{tilt}}$  shows the angle between the debris angular momentum vector and the black hole spin vector, and the nodal angle  $\theta_{\text{prec}}$  shows the angle between the debris angular momentum vector and the z-axis. These two angles are averaged over all SPH particles and normalized by  $2\pi$ . The dashed lines show the nodal angles in the radiatively inefficient cooling cases, and the solid lines denote the nodal angles in the radiatively efficient cooling cases. The dotted lines denote the tilt angles in both cases. Note that the green solid line denotes the nodal angle in the radiatively efficient  $N_{\text{SPH}} = 500\text{K}$  particles' simulation for Model 7. The run time  $t$  is in units of  $P_* = 2\pi\sqrt{r_t^3/GM} \simeq 2.8$  hr.

equation (21), the nodal precession rate per orbit depends almost entirely on the pericentre distance. Orbit-averaged apsidal precession behaves similarly. Debris streams from parabolic TDEs will therefore self-intersect at points very similar to the self-intersection points in the radiatively efficient simulation of Model 1. Also, in our radiatively efficient Models 1-3, we see increasing circularization efficiency with increasing eccentricity; this is largely a function of stream relative velocity at the self-intersection radius. The circularization efficiency can become very low when this radius is comparable to the stream apocentre.

The greater uncertainty in extrapolating our results to the parabolic limit is the structure of the streams, which depends sensitively on internal self-gravity and cooling physics. Modeling stream structure in parabolic TDEs goes beyond the scope of this paper. However, our two extreme cooling regimes have outlined the relevant parameter space: if the stream structure is comparable to or thinner than that in our constant-entropy simulations, then debris circularization will depend sensitively on SMBH spin. If stream structure is closer to our radiatively inefficient limit, then SMBH spin will have very little effect on debris circularization.

As a final topic of discussion, we consider where the energy dissipated by debris circularization goes. Recently, Jiang et al. (2014) showed that vertical advection of radiation caused by magnetic buoyancy transports energy about 50 times faster than does photon diffusion in the super-Eddington, radiation-pressure dominated accretion regimes that characterize realistic TDE disks. The advective cooling timescale in the vertical direction,  $t_{\text{advz}}$ , is thus estimated to be of the order of  $10^7$  s for the typical parameters of equation (8). Therefore,  $t_{\text{cool}} = \min(t_{\text{diff}}, t_{\text{advz}})$  is the cooling timescale.

If we optimistically assume  $t_{\text{cool}} \lesssim t_c$ , then the energy dissipated by shocks during debris circularization will radi-

ate away as thermal emission via optically thick radiative cooling. The resultant  $L_c = \delta\epsilon_{\text{max}}/t_c$  gives an upper limit on the circularization luminosity of parabolic TDEs:

$$\frac{L_c}{L_{\text{edd}}} \simeq 2.1 \times 10^{-1} \left(\frac{\beta}{1}\right) \left(\frac{100}{N_{\text{peri}}}\right) \left(\frac{m_*}{M_{\odot}}\right)^{7/3} \left(\frac{r_*}{R_{\odot}}\right)^{-5/2} \times \left(\frac{M_{\text{BH}}}{10^6 M_{\odot}}\right)^{-5/6} \quad (26)$$

where we adopt  $t_c = N_{\text{peri}} t_{\text{fb}}$  with the number of pericentre passages  $N_{\text{peri}}$  during debris circularization, and  $L_{\text{edd}} = 4\pi G M_{\text{BH}} m_p c / \sigma_T$  is the Eddington luminosity with the proton mass  $m_p$  and the Thomson cross section  $\sigma_T$ . In the cases of eccentric TDEs or radiatively inefficient parabolic ones, this luminosity is reduced by a factor  $t_c/t_{\text{diff}}$ . The actual radiated energy could be further reduced by a transition to a radiatively inefficient cooling flow or by a super-Eddington outflow (Strubbe & Quataert 2011). However, it is clear that the circularization energy budget, especially for parabolic TDEs, is substantial. Such emission could be observed as a precursor to the parabolic TDE flare powered by accretion onto the SMBH for  $M_{\text{BH}} \gtrsim 2 \times 10^6 M_{\odot}$ , where the radiatively efficient scenario is applicable. For typical parameters, the upper limit of the precursor luminosity can be comparable to the Eddington luminosity.

A similar idea was proposed by equation (8) of Boganović et al. (2014) in the context of tidal disruption of a red giant star on a parabolic orbit. However, it is important to evaluate whether the energy dissipated by shocks can actually be radiated away within a fallback time. If this is not the case, then any precursor signal from circularization luminosity will be strongly suppressed as with our radiatively inefficient cooling simulations. We have found that the dissipated energy will be efficiently radiated away for black holes above a critical mass:  $\sim 2 \times 10^6 M_{\odot}$  for electron scattering

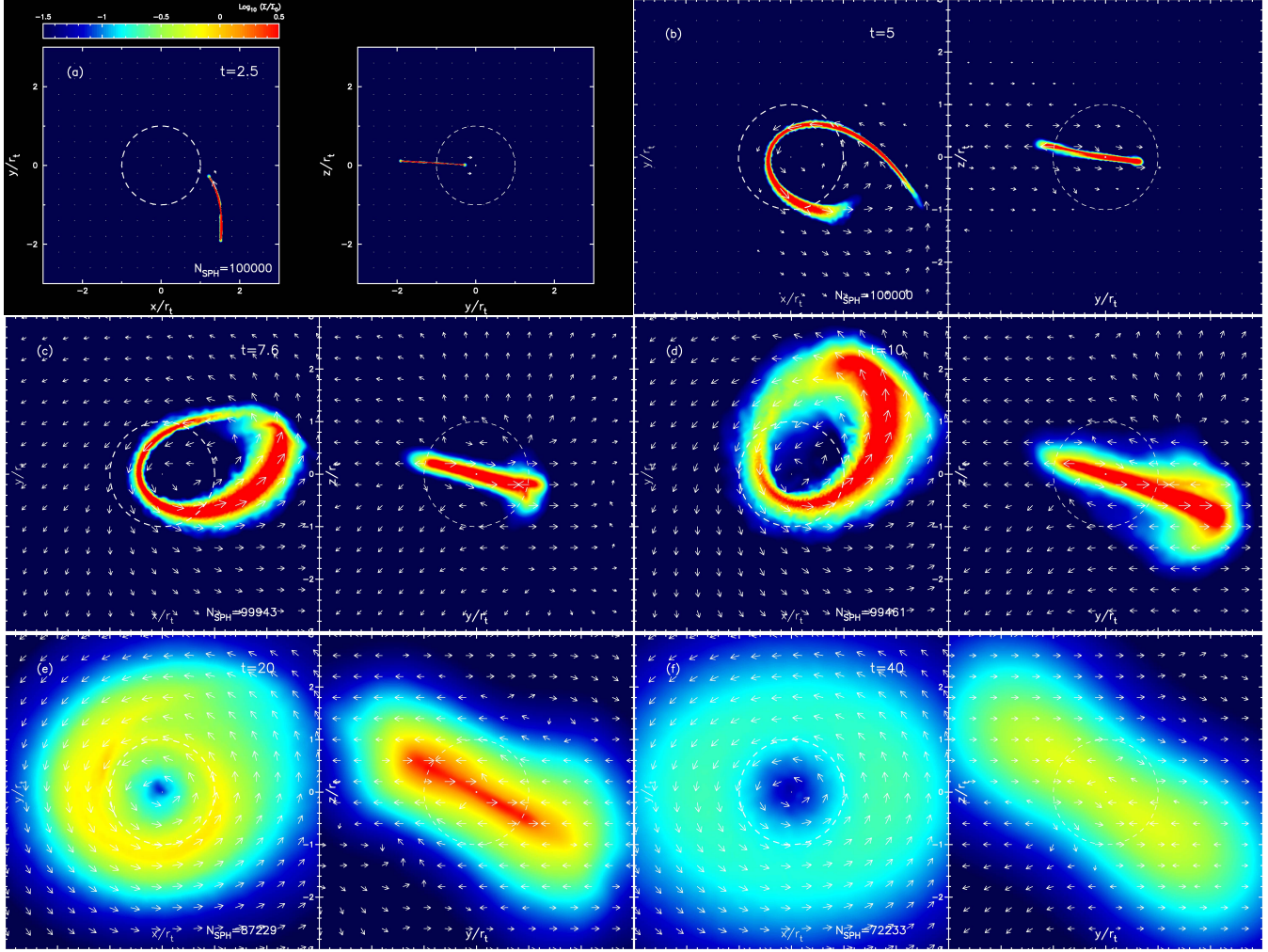


**Figure 18.** A sequence of snapshots of the tidal disruption process in Model 7 ( $a_* = 5/3$ ,  $e_* = 0.7$ ,  $\beta = 2$ ,  $\chi = -0.9$ , and  $i = 90^\circ$ ) in the radiatively inefficient limit. Each panel shows surface densities projected on  $x$ - $y$  plane (left panel) and on  $y$ - $z$  plane (right panel) for  $0 \leq t \leq 40$ . The other figure formats are the same as Figure 5.

opacity. The precursor luminosity can be more accurately obtained by self-consistently calculating the cooling rate of the emitted region of the debris and its stream structure. A more detailed study will be done in the future.

In summary, eccentric TDEs serve as a valuable and computationally tractable testbed for the physics of circularization, which is extremely challenging to simulate for parabolic TDEs around SMBHs. Our first ever simulations of stellar tidal disruption around spinning SMBHs confirm past analytic predictions of disk precession, and indicate that black hole spin may imprint itself, via circularization delays, onto mass fallback rates in parabolic TDEs. Future study of debris stream dynamics in the parabolic limit is required to make more definite predictions, but for now we conclude that SMBH spin is of crucial importance for the circularization of thin debris streams, a process aided by retrograde or aligned spin, and hindered by prograde or misaligned spin.

## APPENDIX A: SIMPLE TREATMENT OF RELATIVISTIC EFFECTS IN SPH

Here we briefly describe how to incorporate PN correction terms relevant for the tidal disruption problem into an existing SPH code. Specifically, we add the PN acceleration terms into the SPH momentum equation, and leave the other SPH equations unchanged.

The SPH momentum equation for the  $i$ -th particle with PN corrections can be written by

$$\begin{aligned} \frac{d\mathbf{v}_i}{dt} = & \sum_j^{N_{\text{nei}}} m_j \left( \frac{P_i}{\rho_i^2} + \frac{P_j}{\rho_j^2} + \Pi_{ij} \right) \nabla_j W(r_{ij}, h_{ij}) \\ & - \sum_j^N \frac{GM(r_{ij})}{r_{ij}^2} \frac{\mathbf{r}_{ij}}{r_{ij}} \\ & + \mathbf{a}_{i,0\text{PN}} + \frac{1}{c^2} \mathbf{a}_{i,1\text{PN}} + \frac{1}{c^3} \mathbf{a}_{i,1.5\text{PN}} + \frac{1}{c^4} \mathbf{a}_{i,2\text{PN}}, \quad (\text{A1}) \end{aligned}$$

where  $P_j$  and  $\rho_j$  are the pressure and density of particle  $j$ , respectively, and  $\Pi_{ij}$  is the standard form of the artificial



viscosity (Bate 1995):

$$\Pi_{i,j} = \begin{cases} (-\alpha_{\text{SPH}} c_s \mu_{ij} + \beta_{\text{SPH}} \mu_{ij}^2) / \rho_{ij} & \mathbf{v}_{ij} \cdot \mathbf{r}_{ij} \leq 0 \\ 0 & \mathbf{v}_{ij} \cdot \mathbf{r}_{ij} > 0. \end{cases} \quad (\text{A2})$$

Here,  $\alpha_{\text{SPH}}$  and  $\beta_{\text{SPH}}$  are linear and nonlinear artificial viscosity parameters, respectively;  $\rho_{ij} = (\rho_i + \rho_j)/2$ ,  $\mathbf{v}_{ij} = \mathbf{v}_i - \mathbf{v}_j$ , and  $\mu_{ij} = h_{ij} \mathbf{v}_{ij} \cdot \mathbf{r}_{ij} / (r_{ij} + \eta_{ij})$  with  $\eta_{ij}^2 = 0.01 h_{ij}^2$ . Note that we adopt the standard values,  $\alpha_{\text{SPH}} = 1$  and  $\beta_{\text{SPH}} = 2$ , for the artificial viscosity parameters in our simulations. The artificial viscosity consists of two terms: the first term that is linear in the velocity differences between particles, which produces a shear and bulk viscosity, and the second term that is quadratic in the velocity differences, which is needed to eliminate particle interpenetration in high Mach number shocks.  $W$  is the weighting function called by kernel. We adopt the standard cubic-spline kernel for 3D (Bate 1995):

$$W(r_{ij}, h_{ij}) = \frac{1}{\pi h^3} \begin{cases} 1 - (3/2)s^2 + (3/4)s^3 & \text{if } 0 \leq s < 1 \\ (2-s)^{3/4} & \text{if } 1 \leq s < 2 \\ 0 & \text{otherwise,} \end{cases} \quad (\text{A3})$$

where  $s = |r_{ij}/h_{ij}|$ .

The second term of right hand side of equation (A1) shows the self-gravitating force acting on particle  $i$  from all the other SPH particles, where

$$M(r_{ij}) = 4\pi \int_0^{r_{ij}} r^2 \rho(r) dr.$$

The third term to the sixth term show the gravitational forces acting on particle  $i$  from the black hole. The Newtonian (0PN), 1PN, and 2PN accelerations among them can be written by (Blanchet 2006)

$$\begin{aligned} \mathbf{a}_{i,0\text{PN}} &= -\frac{GM_{\text{BH}}}{r_{i\text{BH}}^2} \mathbf{n}_{i\text{BH}} \\ \mathbf{a}_{i,1\text{PN}} &= \left[ \frac{5G^2 m_i M_{\text{BH}}}{r_{i\text{BH}}^3} + \frac{4G^2 M_{\text{BH}}^2}{r_{i\text{BH}}^3} \right. \\ &\quad + \frac{GM_{\text{BH}}}{r_{i\text{BH}}^2} \left( \frac{3}{2} (\mathbf{n}_{i\text{BH}} \cdot \mathbf{v}_{\text{BH}})^2 \right. \\ &\quad \left. \left. - v_i^2 + 4(\mathbf{v}_i \cdot \mathbf{v}_{\text{BH}}) - 2v_{\text{BH}}^2 \right) \right] \mathbf{n}_{i\text{BH}} \\ &\quad + \frac{GM_{\text{BH}}}{r_{i\text{BH}}^2} [4(\mathbf{n}_{i\text{BH}} \cdot \mathbf{v}_i) - 3(\mathbf{n}_{i\text{BH}} \cdot \mathbf{v}_{\text{BH}})] \mathbf{v}_{i\text{BH}} \\ \mathbf{a}_{i,2\text{PN}} &= - \left[ \frac{57G^3 m_i^2 M_{\text{BH}}}{4r_{i\text{BH}}^4} + \frac{69G^3 m_i M_{\text{BH}}^2}{2r_{i\text{BH}}^4} \right. \\ &\quad + \frac{9G^3 M_{\text{BH}}^3}{r_{i\text{BH}}^4} \mathbf{n}_{i\text{BH}} + \frac{GM_{\text{BH}}}{r_{i\text{BH}}^2} \left[ -\frac{15}{8} (\mathbf{n}_{i\text{BH}} \cdot \mathbf{v}_{\text{BH}})^4 \right. \\ &\quad + \frac{3}{2} (\mathbf{n}_{i\text{BH}} \cdot \mathbf{v}_{\text{BH}})^2 v_i^2 - 6(\mathbf{n}_{i\text{BH}} \cdot \mathbf{v}_{\text{BH}})^2 (\mathbf{v}_i \cdot \mathbf{v}_{\text{BH}}) \\ &\quad - 2(\mathbf{v}_i \cdot \mathbf{v}_{\text{BH}})^2 + \frac{9}{2} (\mathbf{n}_{i\text{BH}} \cdot \mathbf{v}_{\text{BH}})^2 v_{\text{BH}}^2 \\ &\quad + 4(\mathbf{v}_i \cdot \mathbf{v}_{\text{BH}}) v_{\text{BH}}^2 \\ &\quad \left. \left. - 2v_{\text{BH}}^4 \right] \mathbf{n}_{i\text{BH}} + \frac{G^2 m_i M_{\text{BH}}}{r_{i\text{BH}}^3} \left[ \frac{39}{2} (\mathbf{n}_{i\text{BH}} \cdot \mathbf{v}_i)^2 \right. \right. \\ &\quad \left. \left. - 39(\mathbf{n}_{i\text{BH}} \cdot \mathbf{v}_i)(\mathbf{n}_{i\text{BH}} \cdot \mathbf{v}_{\text{BH}}) + \frac{17}{2} (\mathbf{n}_{i\text{BH}} \cdot \mathbf{v}_{\text{BH}})^2 \right. \right. \end{aligned}$$

$$\begin{aligned} &\quad \left. - \frac{15}{4} v_i^2 - \frac{5}{2} (\mathbf{v}_i \cdot \mathbf{v}_{\text{BH}}) + \frac{5}{4} v_{\text{BH}}^2 \right] \mathbf{n}_{i\text{BH}} \\ &\quad + \frac{GM_{\text{BH}}^2}{r_{i\text{BH}}^3} \left[ \frac{4}{2} (\mathbf{n}_{i\text{BH}} \cdot \mathbf{v}_i)^2 \right. \\ &\quad - 4(\mathbf{n}_{i\text{BH}} \cdot \mathbf{v}_i)(\mathbf{n}_{i\text{BH}} \cdot \mathbf{v}_{\text{BH}}) + 6(\mathbf{n}_{i\text{BH}} \cdot \mathbf{v}_{\text{BH}})^2 \\ &\quad - 8(\mathbf{v}_i \cdot \mathbf{v}_{\text{BH}}) + 4v_{\text{BH}}^2 \left. \right] \mathbf{n}_{i\text{BH}} + \frac{G^2 M_{\text{BH}}^2}{r_{i\text{BH}}^3} \left[ \right. \\ &\quad \left. - 2(\mathbf{n}_{i\text{BH}} \cdot \mathbf{v}_i) - 2(\mathbf{n}_{i\text{BH}} \cdot \mathbf{v}_{\text{BH}}) \right] \mathbf{v}_{i\text{BH}} \\ &\quad + \frac{G^2 m_i M_{\text{BH}}}{r_{i\text{BH}}^3} \left[ -\frac{63}{4} (\mathbf{n}_{i\text{BH}} \cdot \mathbf{v}_i) \right. \\ &\quad + \frac{55}{4} (\mathbf{n}_{i\text{BH}} \cdot \mathbf{v}_{\text{BH}}) \left. \right] \mathbf{v}_{i\text{BH}} \\ &\quad + \frac{GM_{\text{BH}}}{r_{i\text{BH}}^2} \left[ -6(\mathbf{n}_{i\text{BH}} \cdot \mathbf{v}_i)(\mathbf{n}_{i\text{BH}} \cdot \mathbf{v}_{\text{BH}})^2 \right. \\ &\quad + \frac{9}{2} (\mathbf{n}_{i\text{BH}} \cdot \mathbf{v}_{\text{BH}})^3 + (\mathbf{n}_{i\text{BH}} \cdot \mathbf{v}_{\text{BH}}) v_i^2 \\ &\quad - 4(\mathbf{n}_{i\text{BH}} \cdot \mathbf{v}_i)(\mathbf{v}_i \cdot \mathbf{v}_{\text{BH}}) \\ &\quad + 4(\mathbf{n}_{i\text{BH}} \cdot \mathbf{v}_{\text{BH}})(\mathbf{v}_i \cdot \mathbf{v}_{\text{BH}}) \\ &\quad \left. \left. + 4(\mathbf{n}_{i\text{BH}} \cdot \mathbf{v}_i) v_{\text{BH}}^2 - 5(\mathbf{n}_{i\text{BH}} \cdot \mathbf{v}_{\text{BH}}) v_{\text{BH}}^2 \right] \mathbf{v}_{i\text{BH}} \quad (\text{A4}) \end{aligned}$$

where  $\mathbf{r}_{\text{BH}}$  and  $\mathbf{v}_{\text{BH}}$  are the position and velocity vector of the black hole particle, respectively, and  $\mathbf{r}_{i\text{BH}} \equiv \mathbf{r}_i - \mathbf{r}_{\text{BH}}$ ,  $\mathbf{v}_{i\text{BH}} \equiv \mathbf{v}_i - \mathbf{v}_{\text{BH}}$ , and  $\mathbf{n}_{i\text{BH}} \equiv (\mathbf{r}_i - \mathbf{r}_{\text{BH}})/|\mathbf{r}_i - \mathbf{r}_{\text{BH}}|$ . The 1.5PN acceleration due to the black hole spin can be also written by Faye et al. (2007) as

$$\begin{aligned} \mathbf{a}_{i,1.5\text{PN}} &= \frac{GM_{\text{BH}}}{r_{i\text{BH}}^3} \left[ 6 \left( \frac{\mathbf{S}_i \cdot (\mathbf{n}_{i\text{BH}} \times \mathbf{v}_{i\text{BH}})}{m_i} \right. \right. \\ &\quad \left. \left. + \frac{\mathbf{S}_{\text{BH}} \cdot (\mathbf{n}_{i\text{BH}} \times \mathbf{v}_{i\text{BH}})}{M_{\text{BH}}} \right) \mathbf{n}_{i\text{BH}} \right. \\ &\quad + 3(\mathbf{n}_{i\text{BH}} \cdot \mathbf{v}_{i\text{BH}}) \frac{\mathbf{n}_{i\text{BH}} \times \mathbf{S}_i}{m_i} \left. \right] \\ &\quad + \frac{GM_{\text{BH}}}{r_{i\text{BH}}^3} \left[ 6(\mathbf{n}_{i\text{BH}} \cdot \mathbf{v}_{i\text{BH}}) \frac{\mathbf{n}_{i\text{BH}} \times \mathbf{S}_{\text{BH}}}{M_{\text{BH}}} \right. \\ &\quad \left. - 3 \frac{\mathbf{v}_{i\text{BH}} \times \mathbf{S}_i}{m_i} - 4 \frac{\mathbf{v}_{i\text{BH}} \times \mathbf{S}_{\text{BH}}}{M_{\text{BH}}} \right], \quad (\text{A5}) \end{aligned}$$

where  $\mathbf{S}_i$  and  $\mathbf{S}_{\text{BH}}$  are the spin vectors of particle  $i$  and black hole, respectively. In our simulation,  $\mathbf{S}_i = 0$  and  $\mathbf{S}_{\text{BH}} = GM_{\text{BH}}^2 \chi \hat{\mathbf{s}}$  are adopted, where  $\chi$  is the black hole spin parameter with value of  $0 \leq \chi \leq 1$  and  $\hat{\mathbf{s}}$  is the unit vector of spin angular momentum of the black hole.

## A1 Post-Newtonian corrections to binding energy and angular momentum

The binding energy and angular momentum of SPH particles are also corrected by PN approximations. The total binding

energy of the system is given by

$$\mathcal{E} = \sum_{i=1}^{N_{\text{SPH}}} E_i, \quad (\text{A6})$$

where the binding energy of a SPH particle,  $E_i$ , can be corrected (Blanchet 2006; Faye et al. 2007) as

$$E_i = E_{i,0\text{PN}} + \frac{1}{c^2} E_{i,1\text{PN}} + \frac{1}{c^3} E_{i,1.5\text{PN}} + \frac{1}{c^4} E_{i,2\text{PN}}, \quad (\text{A7})$$

where

$$\begin{aligned} E_{i,0\text{PN}} &= \frac{1}{2}(m_i v_i^2 + M_{\text{BH}} v_{\text{BH}}^2) - \frac{Gm_i M_{\text{BH}}}{r_{i\text{BH}}}, \\ E_{i,1\text{PN}} &= -\frac{G^2 m_i^2 M_{\text{BH}}}{2r_{i\text{BH}}^2} + \frac{m_i v_i^4}{8} + \frac{Gm_i M_{\text{BH}}}{r_{i\text{BH}}} \\ &\times \left[ -\frac{1}{4}(\mathbf{n}_{i\text{BH}} \cdot \mathbf{v}_i)(\mathbf{n}_{i\text{BH}} \cdot \mathbf{v}_{\text{BH}}) + \frac{3}{2}v_i^2 \right. \\ &\left. - \frac{7}{4}(\mathbf{v}_i \cdot \mathbf{v}_{\text{BH}}) \right] \\ &- \frac{G^2 M_{\text{BH}}^2 m_i}{2r_{i\text{BH}}^2} + \frac{M_{\text{BH}} v_{\text{BH}}^4}{8} + \frac{GM_{\text{BH}} m_i}{r_{i\text{BH}}} \\ &\times \left[ -\frac{1}{4}(\mathbf{n}_{i\text{BH}} \cdot \mathbf{v}_{\text{BH}})(\mathbf{n}_{i\text{BH}} \cdot \mathbf{v}_i) + \frac{3}{2}v_{\text{BH}}^2 \right. \\ &\left. - \frac{7}{4}(\mathbf{v}_{\text{BH}} \cdot \mathbf{v}_i) \right], \\ E_{i,1.5\text{PN}} &= \frac{GM_{\text{BH}}}{r_{i\text{BH}}^2} [\mathbf{S}_i \cdot (\mathbf{n}_{i\text{BH}} \times \mathbf{v}_i)] \\ &- \frac{Gm_i}{r_{i\text{BH}}^2} [\mathbf{S}_{\text{BH}} \cdot (\mathbf{n}_{i\text{BH}} \times \mathbf{v}_{\text{BH}})], \\ E_{i,2\text{PN}} &= -\frac{G^3 m_i^3 M_{\text{BH}}}{2r_{i\text{BH}}^3} - \frac{19G^3 m_i^2 M_{\text{BH}}^2}{8r_{i\text{BH}}^3} + \frac{5}{16}m_i v_i^6 \\ &- \frac{G^3 M_{\text{BH}}^3 m_i}{2r_{i\text{BH}}^3} - \frac{19G^3 M_{\text{BH}}^2 m_i^2}{8r_{i\text{BH}}^3} + \frac{5}{16}M_{\text{BH}} v_{\text{BH}}^6 \\ &+ \frac{G^2 m_i^2 M_{\text{BH}}}{r_{i\text{BH}}^2} \left[ \frac{29}{4}(\mathbf{n}_{i\text{BH}} \cdot \mathbf{v}_i)^2 \right. \\ &- \frac{13}{4}(\mathbf{n}_{i\text{BH}} \cdot \mathbf{v}_i)(\mathbf{n}_{i\text{BH}} \cdot \mathbf{v}_{\text{BH}}) \\ &+ \frac{1}{2}(\mathbf{n}_{i\text{BH}} \cdot \mathbf{v}_{\text{BH}})^2 - \frac{3}{2}v_i^2 + \frac{7}{4}v_{\text{BH}}^2 \left. \right] + \frac{G^2 M_{\text{BH}}^2 m_i}{r_{i\text{BH}}^2} \\ &\times \left[ \frac{29}{4}(\mathbf{n}_{i\text{BH}} \cdot \mathbf{v}_{\text{BH}})^2 - \frac{13}{4}(\mathbf{n}_{i\text{BH}} \cdot \mathbf{v}_{\text{BH}})(\mathbf{n}_{i\text{BH}} \cdot \mathbf{v}_i) \right. \\ &+ \frac{1}{2}(\mathbf{n}_{i\text{BH}} \cdot \mathbf{v}_i)^2 - \frac{3}{2}v_{\text{BH}}^2 + \frac{7}{4}v_i^2 \left. \right] + \frac{Gm_i M_{\text{BH}}}{r_{i\text{BH}}} \\ &\times \left[ \frac{3}{8}(\mathbf{n}_{i\text{BH}} \cdot \mathbf{v}_i)^3 (\mathbf{n}_{i\text{BH}} \cdot \mathbf{v}_{\text{BH}}) \right. \\ &+ \frac{3}{16}(\mathbf{n}_{i\text{BH}} \cdot \mathbf{v}_i)^2 (\mathbf{n}_{i\text{BH}} \cdot \mathbf{v}_{\text{BH}})^2 \\ &- \frac{9}{8}(\mathbf{n}_{i\text{BH}} \cdot \mathbf{v}_i)(\mathbf{n}_{i\text{BH}} \cdot \mathbf{v}_{\text{BH}})v_i^2 - \frac{13}{8}(\mathbf{n}_{i\text{BH}} \cdot \mathbf{v}_{\text{BH}})^2 v_i^2 \\ &+ \frac{21}{8}v_i^4 + \frac{13}{8}(\mathbf{n}_{i\text{BH}} \cdot \mathbf{v}_i)^2 (\mathbf{v}_i \cdot \mathbf{v}_{\text{BH}}) \\ &+ \frac{3}{4}(\mathbf{n}_{i\text{BH}} \cdot \mathbf{v}_i)(\mathbf{n}_{i\text{BH}} \cdot \mathbf{v}_{\text{BH}})(\mathbf{v}_i \cdot \mathbf{v}_{\text{BH}}) \end{aligned}$$

$$\begin{aligned} &- \frac{55}{8}v_i^2 (\mathbf{v}_i \cdot \mathbf{v}_{\text{BH}}) + \frac{17}{8}(\mathbf{v}_i \cdot \mathbf{v}_{\text{BH}})^2 + \frac{31}{16}v_i^2 v_{\text{BH}}^2 \left. \right] \\ &+ \frac{Gm_i M_{\text{BH}}}{r_{i\text{BH}}} \left[ \frac{3}{8}(\mathbf{n}_{i\text{BH}} \cdot \mathbf{v}_{\text{BH}})^3 (\mathbf{n}_{i\text{BH}} \cdot \mathbf{v}_i) \right. \\ &+ \frac{3}{16}(\mathbf{n}_{i\text{BH}} \cdot \mathbf{v}_{\text{BH}})^2 (\mathbf{n}_{i\text{BH}} \cdot \mathbf{v}_i)^2 \\ &- \frac{9}{8}(\mathbf{n}_{i\text{BH}} \cdot \mathbf{v}_{\text{BH}})(\mathbf{n}_{i\text{BH}} \cdot \mathbf{v}_i)v_{\text{BH}}^2 \\ &- \frac{13}{8}(\mathbf{n}_{i\text{BH}} \cdot \mathbf{v}_i)^2 v_{\text{BH}}^2 + \frac{21}{8}v_{\text{BH}}^4 \\ &+ \frac{13}{8}(\mathbf{n}_{i\text{BH}} \cdot \mathbf{v}_{\text{BH}})^2 (\mathbf{v}_i \cdot \mathbf{v}_{\text{BH}}) \\ &+ \frac{3}{4}(\mathbf{n}_{i\text{BH}} \cdot \mathbf{v}_{\text{BH}})(\mathbf{n}_{i\text{BH}} \cdot \mathbf{v}_i)(\mathbf{v}_i \cdot \mathbf{v}_{\text{BH}}) \\ &\left. - \frac{55}{8}v_{\text{BH}}^2 (\mathbf{v}_i \cdot \mathbf{v}_{\text{BH}}) + \frac{17}{8}(\mathbf{v}_i \cdot \mathbf{v}_{\text{BH}})^2 + \frac{31}{16}v_i^2 v_{\text{BH}}^2 \right]. \end{aligned}$$

The total angular momentum vector of the system can be written by

$$\mathcal{J} = \sum_{i=1}^{N_{\text{SPH}}} \mathbf{J}_i, \quad (\text{A8})$$

where the angular momentum vector of a SPH particle,  $\mathbf{J}_i$ , is corrected by de Andrade et al. (2001); Faye et al. (2007) as

$$\mathbf{J}_i = \mathbf{J}_{i,0\text{PN}} + \frac{1}{c^2} \mathbf{J}_{i,1\text{PN}} + \frac{1}{c^3} \mathbf{J}_{i,1.5\text{PN}} + \frac{1}{c^4} \mathbf{J}_{i,2\text{PN}}. \quad (\text{A9})$$

Here, each term of the right-hand side can be written as the ingredient-label format by

$$\begin{aligned} J_{i,0\text{PN}}^l &= \varepsilon_{lmn} (m_i r_i^m v_i^n + M_{\text{BH}} r_{\text{BH}}^m v_{\text{BH}}^n) \\ J_{i,1\text{PN}}^l &= \varepsilon_{lmn} \left[ r_i^m v_i^n \left( \frac{3Gm_i M_{\text{BH}}}{r_{i\text{BH}}} + \frac{m_i v_i^2}{2} \right) \right. \\ &- r_i^m v_{\text{BH}}^n \frac{7Gm_i M_{\text{BH}}}{2r_{i\text{BH}}} + r_i^m r_{\text{BH}}^n \frac{Gm_i M_{\text{BH}}}{2r_{i\text{BH}}^2} (\mathbf{n}_{i\text{BH}} \cdot \mathbf{v}_i) \left. \right] \\ J_{i,2\text{PN}}^l &= \varepsilon_{lmn} \left\{ -v_i^m v_{\text{BH}}^n \frac{7Gm_i M_{\text{BH}}}{4} (\mathbf{n}_{i\text{BH}} \cdot \mathbf{v}_i) \right. \\ &+ r_i^m v_i^n \left[ -\frac{5G^2 m_i^2 M_{\text{BH}}}{4r_{i\text{BH}}^2} + \frac{7G^2 m_i M_{\text{BH}}^2}{2r_{i\text{BH}}^2} \right. \\ &+ \frac{3m_i v_i^4}{8} + \frac{Gm_i M_{\text{BH}}}{r_{i\text{BH}}} \left( -\frac{3}{2}(\mathbf{n}_{i\text{BH}} \cdot \mathbf{v}_{\text{BH}})^2 + \frac{7}{2}v_i^2 \right. \\ &- 4(\mathbf{v}_i \cdot \mathbf{v}_{\text{BH}}) + 2v_{\text{BH}}^2 \left. \right) \left. \right] + r_i^m v_{\text{BH}}^n \left[ -\frac{7G^2 m_i M_{\text{BH}}^2}{4r_{i\text{BH}}^2} \right. \\ &+ \frac{Gm_i M_{\text{BH}}}{r_{i\text{BH}}} \left( -\frac{1}{8}(\mathbf{n}_{i\text{BH}} \cdot \mathbf{v}_i)^2 \right. \\ &- \frac{1}{4}(\mathbf{n}_{i\text{BH}} \cdot \mathbf{v}_i)(\mathbf{n}_{i\text{BH}} \cdot \mathbf{v}_{\text{BH}}) + \frac{13}{8}(\mathbf{n}_{i\text{BH}} \cdot \mathbf{v}_{\text{BH}})^2 \\ &- \frac{9}{8}v_i^2 + \frac{9}{4}(\mathbf{v}_i \cdot \mathbf{v}_{\text{BH}}) - \frac{23}{8}v_{\text{BH}}^2 \left. \right] + r_i^m r_{\text{BH}}^n \left[ \frac{G^2 m_i^2 M_{\text{BH}}}{r_{i\text{BH}}^3} \right. \\ &\times \left( -\frac{29}{4}(\mathbf{n}_{i\text{BH}} \cdot \mathbf{v}_i) + \frac{9}{4}(\mathbf{n}_{i\text{BH}} \cdot \mathbf{v}_{\text{BH}}) \right) + \frac{Gm_i M_{\text{BH}}}{r_{i\text{BH}}^2} \\ &\times \left( -\frac{3}{8}(\mathbf{n}_{i\text{BH}} \cdot \mathbf{v}_i)^3 - \frac{3}{8}(\mathbf{n}_{i\text{BH}} \cdot \mathbf{v}_i)^2 (\mathbf{n}_{i\text{BH}} \cdot \mathbf{v}_{\text{BH}}) \right. \end{aligned}$$

$$+ \frac{9}{8}(\mathbf{n}_{\text{BH}} \cdot \mathbf{v}_i)v_i^2 + \frac{7}{8}(\mathbf{n}_{\text{BH}} \cdot \mathbf{v}_{\text{BH}})v_i^2 - \frac{7}{4}(\mathbf{n}_{\text{BH}} \cdot \mathbf{v}_i)(\mathbf{v}_i \cdot \mathbf{v}_{\text{BH}}) \Big) \Big] \Big\}, \quad (\text{A10})$$

where  $\varepsilon_{lmn}$  shows Levi-Civita tensor with  $(l, m, n = 1, 2, 3)$ , and the spin term can be written as a vector format by

$$\begin{aligned} \mathbf{J}_{i,1.5\text{PN}} &= -\frac{GM_{\text{BH}}}{r_{\text{BH}}^2} \mathbf{r}_i \times (\mathbf{n}_{\text{BH}} \times \mathbf{S}_i) \\ &+ \frac{Gm_i}{r_{\text{BH}}^2} \mathbf{r}_{\text{BH}} \times (\mathbf{n}_{\text{BH}} \times \mathbf{S}_{\text{BH}}) \\ &+ \frac{GM_{\text{BH}}}{r_{\text{BH}}} [2(\mathbf{n}_{\text{BH}} \cdot \mathbf{S}_i) \cdot \mathbf{n}_{\text{BH}} - \mathbf{S}_i] + \frac{1}{2}v_i^2 \mathbf{S}_i \\ &- (\mathbf{v}_i \cdot \mathbf{S}_i) \mathbf{v}_i \\ &+ \frac{Gm_i}{r_{\text{BH}}} [2(\mathbf{n}_{\text{BH}} \cdot \mathbf{S}_{\text{BH}}) \cdot \mathbf{n}_{\text{BH}} - \mathbf{S}_{\text{BH}}] + \frac{1}{2}v_{\text{BH}}^2 \mathbf{S}_{\text{BH}} \\ &- (\mathbf{v}_{\text{BH}} \cdot \mathbf{S}_{\text{BH}}) \mathbf{v}_{\text{BH}}. \end{aligned} \quad (\text{A11})$$

## ACKNOWLEDGMENTS

The authors thank to the anonymous referee for fruitful comments and suggestions. K.H. is grateful to Atsuo. T Okazaki and Jongsoo Kim for their helpful discussions and continuous encouragement. K.H. would also like to thank the Kavli Institute for Theoretical Physics (KITP) for their hospitality and support during the program on A Universe of Black Holes. During the completion of this paper, we became aware of complementary numerical simulations by Amaro-Seoane et al. (in prep), but both efforts have proceeded independently. Numerical simulations and data reductions reported here were performed by using a high performance computing cluster (Polaris) at the Korea Astronomy and Space Science Institute and by using computer facilities at Department of Astronomy, Kyoto University, and Harvard-Smithsonian Center for Astrophysics, Harvard University. This work was supported in part by the research grants of the Chungbuk National University in 2015 and Korea Astronomy and Space Science Institute in 2016 [K. H.], the Alfred P. Sloan Foundation through a grant to Brian Metzger [N. S.], and NSF grant AST-1312034 [A. L.].

## REFERENCES

- Ayal S., Livio M., Piran T., 2000, *ApJ*, 545, 772  
 Arcavi I. et al., 2014, *ApJ*, 793, 38  
 Bardeen. J. M., Petterson, J. A., 1975, *ApJ*. 195, L65  
 Bardeen, J. M., Press, W. H., Teukolsky, S. A., 1972, *ApJ*. 178, 347  
 Bate, M. R., Bonnel, I. A., Price, N.M., 1995, *MNRAS*, 277, 362  
 Bate, M. R., 1995, Ph.D. Thesis, ch.2, 30-31  
 Benz W., 1990, in the Numerical Modeling of Nonlinear Stellar Pulsations: Problems and Prospects, ed. Buchler, R.J. (Dordrecht: Kluwer Academic Publishers), 269  
 Benz, W., Bowers, R.L., Cameron, A.G.W., Press, W.H., 1990, *ApJ*, 348, 647  
 Berti, E., Volonteri, M., 2008, *ApJ*, 684, 822  
 Blanchet, L., 2006, *Living. Rev. Relativity*, 9, 4  
 Blanchet, L., Damour, T., Schafer, G., 1990, *MNRAS*, 242, 289  
 Blandford, R. D., Znajek, R. L., 1977, *MNRAS*, 179, 433  
 Bloom J. S. et al., 2011, *Science*, 333, 203  
 Bogdanović, T., Cheng, R. M., Amaro-Seoane, P., 2014, *ApJ*, 788, 99  
 Bonnerot, C., Rossi, M. E., Lodato, G., Price, J. D., 2015, *arXiv:1501.04635*  
 Burrows D. N. et al., 2011, *Nature* 476, 421  
 Cannizzo, J. K., Lee, H. M., Goodman, J., 1990, *ApJ*, 351, 38  
 de Andrade, V. C., Blanchet, L., Faye, G., 2001, *Class. Quantum Grav*, 18, 753  
 Doeleman, S. S., et al., 2012, *Science*, 338, 355  
 Donley J. L., Brandt W. N., Eracleous M., Boller T., 2002, *AJ*, 124, 1308  
 Evans C.R., Kochanek C.S., 1989, *ApJ*, 346, L13  
 Faye, G., Blanchet, L., Buonanno, A., 2007, *arXiv:0605139*  
 Fragile, P. C., Anninos, P., 2005, *ApJ*, 623, 347  
 Fragile, P. C., Blaes, O. M., Anninos, P., J. D. Salmonson., 2007, *ApJ*, 668, 417  
 Franchini A., Lodato G., Facchini S., 2016, *MNRAS*, 455, 1946  
 Gezari S. et al., 2012, *Nature*, 485, 217  
 Genzel, R., et al., 2003, *Nature* 425, 934  
 Guillochon, J., Manukian, H., Ramirez-Ruiz, E., 2014, *ApJ*, 783, 23  
 Hayasaki, K., Stone, N., Loeb, A., 2013, *MNRAS*, 434, 909  
 Holoien, T. W.-S., et al. 2014, *MNRAS*, 445, 3263  
 Jiang, Y.-F., Stone, J. M., Davis, S. W., 2014, *ApJ*, submitted.  
 Kato, S., Fukue, J., Mineshige, S., 2008, (Kyoto: Kyoto University Press), *Black-Hole Accretion Disks Towards a New Paradigm*  
 King A. R., Pringle J. E., 2006, *MNRAS*, 373, L90  
 Kochanek, C. S., 1994, *ApJ*, 422, 508  
 Koide, S., Shibata, K., Kudoh, T., Meier, D. L., 2002, *Science* 295, 1688  
 Komossa S., Bade N., 1999, *A&A*, 343, 775  
 Kormendy, J., Richstone, D., 1995, *ARA&A*, 33, 581  
 Kormendy, J., Ho, L. C., 2013, *ARA&A*, 51, 511  
 Levan, A. J. et al., 2011, *Science*, 333, 199  
 Lodato, G., Rossi, E. M., 2011, *MNRAS*, 410, 359  
 Lodato, G., Price, D., 2010, *MNRAS*, 405, 1212  
 Loeb, A., Ulmer, A., 1997, *ApJ*, 489, 573  
 Magorrian, J., Tremaine, S., Richstone, D., et al, 1998, *AJ* 115, 2285  
 Magorrian, J., Tremaine, S., 1999, *MNRAS*, 309, 447  
 McKinney, J. C., Tchekhovskoy, A., Blandford, R. D., *Science*, 2013, 339, 49  
 Merritt, D., Alexander, T., Mikkola, S., Will, C. M. 2011, *PRD*, 81, 6, 062002  
 Mihalas, D., Mihalas, B. W. 1984, *Foundations of radiation hydrodynamics*, ed. Mihalas, D. & Mihalas, B. W.  
 Miller, J. M., 2007, *ARA&A*, 45, 441  
 Miyoshi, M., et al., 1995, *Nature* 373, 127  
 Nelson, R. P., Papaloizou, J. C. B., 2000, *MNRAS*, 315, 570  
 Ogilvie, G. 1999, *MNRAS*, 304, 557  
 Papaloizou, J. C. B., & Pringle, J. E. 1983, *MNRAS*, 202, 1181  
 Ramirez-Ruiz, E., Rosswog, S., 2009, *ApJ*, 697, 77

- Rees, M. J., 1998, *Nature* 333, 523  
Risaliti, G., et al., 2013, *Nature* 452, 449  
Schödel, R., et al, 2002, *Nature*, 419, 694  
Stone, N., Loeb, A., 2012, *Physical Review Letters*, 108, 061302  
Stone, N., Sari, R., Loeb, A., 2013, *MNRAS*, 435, 1809  
Stone, N., Metzger, B. D., 2014, arXiv:1410.7772  
Stone, N., Hayasaki, K., Loeb, A., 2015, in prep.  
Strubbe, L. E., Quataert, E., 2011, *MNRAS*, 415, 168  
Tanaka, Y., et al., 1995, *Nature* 375, 659  
Tchekhovskoy, A., McKinney, J. C., 2012, *MNRAS*, 423, L55  
van Velzen, S., Farrar, G. R., 2014, *ApJ*, 792, 53  
Vinkó, J., et al., 2015, *ApJ*, 798, 12  
Volonteri, M., Madau, P., Quataert, E., Rees, M. J., 2005, *ApJ*, 620, 69  
Wang, J., Merritt, D., 2004, *ApJ*, 600, 149  
Wegg, C., 2012, *ApJ*, 749, 183  
Zauderer B. A., et al., 2011, *Nature* 476, 425